

# Optimized segmentation and classification for liver tumor segmentation and classification using opposition-based spotted hyena optimization

Munipraveena Rela<sup>1</sup> | Suryakari Nagaraja Rao<sup>2</sup> | Patil Ramana Reddy<sup>3</sup>

<sup>1</sup>Department of Electronics and communication Engineering, Jawaharlal Nehru Technological University Anantapur, India

<sup>2</sup>Department of Electronics and Communication Engineering, G Pulla Reddy Engineering College(Autonomous), Kurnool, India

<sup>3</sup>Department of Electronics & Communication Engineering, JNTUA College of Engineering, Ananthapuramu, India

## Correspondence

Munipraveena Rela, Research Scholar,  
 Department of Electronics and  
 communication Engineering, Jawaharlal  
 Nehru Technological University  
 Anantapur, India  
 Email: chagpraveena@gmail.com

## Abstract

In today's world, liver cancers are one of the mainly popular cancers occurring in the human body. The greater part of liver carcinomas is more prone to alcohol-related hepatitis and cirrhosis conditions. Moreover, there is another form of cancer namely, metastatic liver cancer, where the tumor is initiated from other organs and extends to the liver. Early and premature diagnosis of liver cancer is necessary as it tends to improvise life expectancy. Nowadays, discriminating the liver and tumor parts from medical images with the aid of completely automated computer-aided software is a more challenging task, since the liver disease can vary from person to person. This article attempts to implement the novel liver tumor segmentation and classification model using the optimization driven segmentation and classification model. The developed model carries out the task in five steps (a) Pre-processing, (b) liver segmentation, (c) tumor segmentation, (d) feature extraction, and (e) classification. At first, the gathered CT images are subjected to pre-processing with three steps that follow contrast enhancement by histogram equalization and noise filtering by the median filter. Next to the pre-processing of the image, the liver is

**Abbreviations:** ACM, active contour model; ADCs, adenocarcinomas; ANNs, artificial neural networks; BOSA, binary orientation search algorithm; CAD, computer aided diagnosis; CNN, convolutional neural network; CT, computed tomography; DT, decision tree; DWT-SVD, discrete wavelet transform-singular value decomposition; 3D FRN, 3D fractal residual network; ED-SHO, economic dispatch-spotted hyena optimizer; ELM, extreme learning machine; EPO, emperor penguin optimizer; FCN, fully convolutional networks; FDR, false discovery rate; FFCM, fast Fuzzy C-mean algorithm; FNR, false negative rate; FPR, false positive rate; FTS, Fuzzy time series; GLCM, gray-level co-occurrence matrix; GRU, gated recurrent units; GWO, Grey Wolf optimization; HCC, hepatocellular carcinoma; HOFTSM, high-order fuzzy time series model; HOFTSLPM, high-order fuzzy time series-linear programming model; HPSSHO, hybrid particle swarm and spotted hyena optimizer; HRMF-EM, hidden random Markov Fields-expectation maximization algorithm; LBP, local binary pattern; LCSH, local cumulative spectral histograms; LSTM, long short term memory; MCC, Matthew's correlation coefficient; MCG, multi-scale candidate generation technique; MET, metastatic carcinoma; MLP, multilayer perceptron; MOSHEPO, multi-objective spotted hyena and emperor penguin optimizer; MOSHO, multi-objective spotted hyena optimizer; NB, Naive Bayes; NMF, non-negative matrix factorization; NN, neural network; NPV, negative predictive value; NS, neutrosophic sets; O-SHO, opposition-based spotted hyena optimization; PD-NETs, poorly-differentiated neuroendocrine tumors; PSO, particle swarm optimization; RNN, recurrent neural network; ROI, region of interest; RSRSIs, remotely sensed high-resolution satellite images; SDF, signed distance function; SFCM, spatial Fuzzy C-means; SFPC, supervised Fuzzy pixel classification; SHO, Spotted hyena optimization; SOA, seagull optimization algorithm; STOA, sooty tern optimization algorithm; SVM, support vector machine; TSA, tunicate swarm algorithm; WD-NETs, well-differentiated NETs; WOA, whale optimization algorithm.

segmented from the CT abdominal image using adaptive thresholding pursued by level set segmentation. Further, a modified algorithm termed as Fuzzy Centroid-based Region Growing Algorithm with tolerance optimization is developed and used for the tumor segmentation. From the segmented tumor image, three sets of features like gray-level co-occurrence matrix (GLCM), shape features, and local binary pattern (LBP) is utilized for the classifier training. In the classification side, two deep learning algorithms are used: recurrent neural network (RNN), and convolutional neural network (CNN). The tumor segmented image is given as input to the CNN, and the extracted features are given as input to the RNN. As an improvement, an optimized hybrid classifier is adopted for the hidden neuron optimization. Moreover, an improved meta-heuristic algorithm called opposition-based spotted hyena optimization (O-SHO) is introduced to perform the optimized segmentation and classification. The experimental results show that the overall accuracy attained by the proposed model is efficient, less sensitive to noise, and performs superior on a diverse set of CT images.

#### KEY WORDS

abdominal CT images, and convolutional neural network, fuzzy centroid-based optimized region growing algorithm, hybrid classifier, liver tumor, liver tumor segmentation and classification, opposition-based spotted hyena optimization, recurrent neural network

## 1 | INTRODUCTION

In this world, the animals and vertebrates are aided by the fundamental functions procured by the liver. The liver disease in the human body provides no prior information and may cause a life-threatening situation. In this case, early detection of liver disease is quite necessary for enhancing the patient's condition. Liver tumors can be considered as one of the frequently occurring internal malignancies in the whole world and it also has a high fatality rate. The early detection and right staging of liver cancer are significant problems in radiography. Based on the report given by the USA, liver cancer is the tenth most general cause of cancer and the fifth and ninth common reasons for cancer mortality in men and women, respectively.<sup>1</sup> Most of the cancer diseases have more survival rate when it is detected in the early stage.<sup>2</sup> CT is one of the significant and best imaging approaches to detect liver tumors.<sup>3,4</sup> Also, CT offers images of the whole liver by "multi-phase sequential scans" after injecting contrast media.<sup>5</sup> During the CT scan, manual segmentation is more complex and hence consumes more time for carrying out the clinical program.

In image processing, segmentation is an important and required procedure that is one of the quite compound tasks.<sup>6,7</sup> Owing to the diverse factors such as the irregular size and shape of the liver in different subjects,

the automatic segmentation of the tumor region from the liver is considered as a challenging point. Moreover, the intensity of the liver seems to be similar amidst the other connected organs like the stomach and spleen, and contrast and blurry edged images.<sup>8,9</sup> In addition, the automatic segmentation of tumors from the liver region faces difficulty due to image with low contrast and vague shape of the lesion.<sup>10,11</sup> The image segmentation approaches like active contrast segmentation, conventional segmentation technique, watershed model, and region growing have some specific challenges like high sensitivity to noise outliers, and over and under segmentation, hence these schemes may yield less accurate results for small computation time.<sup>12,13</sup>

Manual segmentation and classification of liver lesions from the CT images is a tedious task, as the specific lesions like hemangioma and metastasis have a similar appearance as the liver, and thus the manual segmentation task leads to the confusion resulting in less accurate results.<sup>14</sup> Hence, there is an emergent need in developing automated ways of assisting radiologists in the detection of liver lesions from CT images.<sup>15</sup> In the past decades, automatic liver analysis consists of "lesion detection, liver segmentation, lesion classification, and follow-up."<sup>16</sup> In medical image processing, a deep learning model like CNN plays a major role in accurate classification of the medical images.<sup>17</sup> The CNN has an

effective deep learning structure paving to accurate learning. With the help of the convolution procedure on CNN, the extracted features of input data are automatically transferred to the upcoming layers with the help of various hidden units. Moreover, this convolution procedure can also be employed to acquire the important features from the image.<sup>18</sup> In the CNN, the units have a multi-layered structure and a specific procedure is adopted in each layer for releasing the information to the subsequent layer. However, CNN methods require more capability as they operate at a pixel level on images. Besides this, there is a major challenge in the medical imaging domain. The availability of the sufficient amount of annotated information related to the liver tumors of every individual related to the medical task and application region is very rare. In recent times, many datasets such as TCGA-LIHC, Sliver'07, MIDAS, 3DIRCADb, and LiTS dataset in the medical area have become freely accessible as a part of various competitions.

The main contribution pertains to liver tumor segmentation and classification is given as follows:

- To present the fully automatic liver tumor segmentation and classification for the accurate and robust segmentation of tumors, as an essential part of the clinical diagnosis.
- To overwhelm the problem of segmentation of liver and tumor segmentation from the abdominal CT images from various connecting organs. Liver segmentation is accomplished with the aid of adaptive thresholding and level set algorithm.
- While undergoing the region-based segmentation, the entire pixels of the image must be gathered and clustered as a region. In order to perform such grouping, it is required to choose a seed point with the consideration of criteria like intensity, color, texture, and so forth. Hence, the problem related to seeded region growing is to select the optimal initial seed for attaining better segmentation. Here, the performance of segmentation is improved by the modified region growing algorithm, in which the seed point is selected by FCM clustering, and tolerance is tuned by the proposed O-SHO.
- For enhancing the classification accuracy, and minimizing the detection error and computational complexity of conventional classifiers, the performance of classification is improved by optimizing the number of hidden neurons of RNN and CNN classifiers by the developed O-SHO algorithm.

The entire article is arranged in the following manner: Section 2 shows the works related to existing liver tumor segmentation and classification approaches. Liver

tumor segmentation and classification: developed methodology architecture is described in Section 3. Section 4 briefly describes the tumor segmentation and feature extraction techniques used for the effective training of the hybrid classifier. The proposed improved spotted hyena optimization for enhancing the performance of the hybrid classifier is shown in Section 5. Finally, the experimental results are demonstrated in Section 6. At last, the conclusion of the article is shown in Section 7.

## 2 | LITERATURE REVIEW

### 2.1 | Related works

In 2010, Smeets et al<sup>19</sup> have presented SFPC for facilitating the semi-automatic segmentation of liver metastases and tumors in CT images. For continuing the cancer treatment, the precise and well segmented images of the tumors were required. The level set model was developed for the development of the speed image, which was resulted from the classification of pixels by statistical method by supervised learning. The approach has experimented with CT images of the abdomen. The suggested technique was superior in diagnosing liver tumors.

In 2017, Chang et al<sup>20</sup> have suggested a CAD model for diagnosing liver cancer from the tumor features attained from multi-phase CT images. The evaluation of the developed method was conducted on “71 histologically-proven liver tumors,” which consisted of “49 benign and 22 malignant lesions.” By using region growing algorithm, tumors were recognized from the CT image. Further, features such as kinetic curve, shape, and texture were extracted. The results have shown that the suggested model outperformed conventional models for images having to differentiate benign and malignant tumors. To classify the tumors from the non-tumor region, binary logistic regression analysis was performed.

In 2017, Das et al<sup>21</sup> have developed an automatic technique, which combined the spatial fuzzy clustering method and adaptive thresholding to detect cancer region in liver CT images. The developed model has experimented on 123 original images gathered from distinct manually collected datasets. By using adaptive thresholding, the liver part of the CT image was separated from their main parts and later the cancerous regions in the image were segmented using the spatial fuzzy clustering approach. From the segmented cancerous region, the informative features were taken out and they were categorized into two kinds of liver cancers such as MET and HCC by using the MLP and DT classifiers. The approach provided the cancer diagnosis effectively

by attaining high accuracy with the DT classifier. Thus, the outcomes have shown that the SFCM based segmentation with the C4.5 DT classifier was an intelligent method to identify liver cancer automatically.

In 2017, Chaieb et al<sup>22</sup> have presented a segmentation approach for the cancer diagnosis of the four-phase CT images, which was based on the accumulation of the "Expectation-Maximization model and Hidden Markov Random Fields." The spatial data were considered by the latter using voxel neighbors of two contrast phases. Moreover, the technique for segmentation was implemented on a volume of interest, which reduced the processed voxels count. The classification phase was followed by the segmentation phase, and the method namely, Bootstrap resampling was employed. The method includes the random selection of an optimal representative voxels set for classifying the tumor and the non-tumor regions. The proposed model was validated on three medical datasets. It has been proven that the suggested method performed well on the public datasets and the proposed approach had high performance regarding the accuracy, even though the computational time was decreased during the classifier training. The reduced computational time had minimal influence on classifier efficiency.

In 2017, Kange et al<sup>23</sup> have aimed to recognize the various features of CT images through colorectal PD-NETs from WD-NETs and ADCs. The major variables were evaluated from the images by multivariate and univariate evaluations for the diagnosis. Evaluation based on the Receiver operating characteristic has shown the optimal cut-off value of the size of the lymph node as well as tumor, and hence the classification was highly effective. Finally, it had been concluded that the colorectal PD-NETs can be employed for the diagnosis due to its unique characteristics than the WD-NETs.

In 2018, Anter and Hassenian<sup>24</sup> have introduced an enhanced segmentation method for diagnosing the abdominal CT liver tumor images, and the scheme relied on methods like "NS, FFCM, and PSO." The pixel values with high frequencies and intensity of the actual images were eliminated by the median filtering technique in the initial stage for improving the contrast. For assessing the indeterminacy in the NS domain, entropy was employed in the proposed segmentation technique. Later, the NS image was sent to the optimized FFCM by the PSO approach for clustering. For segmenting and clustering tumors, these segmented livers were subjected to the PSOFCM approach. The test results revealed that the overall accuracy obtained by NS was accurate, less sensitive to noise, and consumption of time was also very less. The proposed segmentation scheme performed well on non-uniform CT images.

In 2018, Zheng et al<sup>25</sup> have introduced an automatic approach for segmenting liver tumor in abdominal images taken from CT scans with FCN and NMF based deformable approach. For segmenting liver and tumor, the FCN was trained by the pre-processed data using BM3D. The segmented regions of the liver and tumor were employed as the ROI and the "NMF-based tumor refinement" was initialized. The surfaces of tumors were purified by a 3D deformable technique developed from NMF and were driven using LCSH. The clearance was modeled for acquiring an accurate, smooth, and original liver tumor surface. For the evaluation, 11 medical datasets were used for analyzing the proposed method. The result has shown that the suggested technique was superior to conventional techniques.

In 2019, Dongantekin et al<sup>6</sup> have suggested a hybrid model of "CNN and DWT-SVD based perceptual hash function." The suggested model was modeled to classify the masses from liver CT images as benign or malignant. The significant features essential for categorization were attained using the salient features acquisition with perceptual hash functions. Finally, the results have shown that obtaining the CNN features from images enhanced the classification performance with ELM using various classifiers.

In 2019, Anter and Hassenian<sup>26</sup> have presented an improved segmentation technique based on the watershed algorithm, NS and FFCM to segment CT liver tumor. The values about the intensity were altered and high frequencies were eliminated by median filtering and the histogram equalization method was employed for enhancing the brightness of the CT images. Next, the transformation of the CT image to the NS domain was done with the help of three subsets. The acquired NS image was improved using morphological operators and the adaptive threshold for concentrating on liver parenchyma. The outcomes have proven that the accuracy attained by the NS was less sensitive to noise, accurate, and had less time consumption.

In 2019, Bai et al<sup>27</sup> have introduced a liver tumor segmentation approach for segmenting CT images by MCG, ACM, and 3D FRN in a rough to fine manner. To acquire tumor candidates, the livers were segmented by 3D U-Net, and later MCG was carried out on these regions. Further, to determine tumor regions, 3D FRN was implemented that was taken as coarse segmentation outcomes. At last, for tumor segmentation refinement, ACM was employed. By using 110 cases in the LiTS dataset, the developed 3D MCG-FRN + ACM was trained. Thus, the results have shown that the suggested method was suitable for detecting liver tumors.

In 2017, Gaurav Dhiman and Vijay Kumar<sup>28</sup> have proposed SHO to inspire the hunting behaviors of spotted

hyenas. The three fundamental steps of the classical SHO are to search, encircle, and attack the prey. It is used for solving real-life optimization problems, but it requires less computational efforts to find the optimum solutions. In 2018, Gaurav Dhiman and Vijay Kumar<sup>29</sup> have proposed EPO, which mimics the huddling behavior of emperor penguins. It can generate the huddle boundary, compute temperature around the huddle, calculate the distance, and find the effective mover. It is easy to solve constrained and unconstrained design problems using EPO. But, the algorithm faces high convergence and computational complexity. In 2018, Gaurav Dhiman and Vijay Kumar<sup>30</sup> have proposed MOSHO algorithm for optimizing the multiple objectives problems through the heuristic approach. The roulette wheel mechanism is used to select the effective solutions from the archive and it simulates the social and hunting behaviors of spotted hyenas. The advantages of these techniques are local optima avoidance and the gradient-free mechanism that made them applicable to real-world problems. But, the algorithm needs to improve on its detection time. In 2018, Pritpal Singh and Gaurav Dhiman<sup>31</sup> have developed FTS to obtain granular intervals. It is more advantageous and expert in providing robust, cost-effective, and approximate solutions. However, it should be carried out in a reasonable environment, rather than in an expensive or a complicated manner. In 2018, Gaurav Dhiman and Amandeep Kaur<sup>32</sup> have modeled SHO to inspire the social behaviors of spotted hyenas. It consists of three steps namely searching for prey, encircling, and attacking prey. It is an efficient optimizer to analyze the exploration and exploitation phases of the optimization. Moreover, the results of engineering design problems demonstrate the applicability of the SHO algorithm on the high dimensional environment using low computational efforts.

In 2019, Gaurav Dhiman and Vijay Kumar<sup>33</sup> have developed SOA for solving computationally expensive problems. It can solve large scale constrained problems and high dimensionality bound-constrained real time problems but, it is difficult to define initial design parameters. In 2018, Gaurav Dhiman and Vijay Kumar<sup>34</sup> have proposed SHO for solving complex and nonlinear constrained engineering problems. It generates better quality solutions and gives stable convergence, but in some cases, it takes more time to execute. In 2018, Pritpal Singh, and Gaurav Dhiman<sup>35</sup> have introduced RSHRSIs. It represents the uncertain changes in the form of fuzzy set operators, such as max and min functions. It is applicable in retrieving various information and also useful to locate the regions of uncertain changes. However, RSHRSIs implementation is more complex and difficult. In 2018, Gaurav Dhiman and Amandeep Kaur<sup>36</sup> have proposed HPSSHO to improve the hunting strategy of SHO. It

reduces computational complexity by producing multiple solutions in a single simulation run, and getting information on non-dominated solutions. It does not require a good initial point to perform the search space. In 2018, Gaurav Dhiman and Amandeep Kaur<sup>37</sup> have proposed SHO. It is based on the law of gravitation and simulates the social behavior of spotted hyenas. It is an efficient optimizer to solve the problems and to generate near-optimal designs. Moreover, it is not well at exploring the search space, and also has a more complicated system. In 2018, Amandeep Kaur et al<sup>38</sup> have presented the contemporary quantum behaved approach, which is based on the Schrodinger equation and Monte Carlo method. The power of quantum computing allows for solving the problems that are not feasible on classical computers and thus suggests a considerable speed up to the best known classical approaches. This approach is tested for solving the dynamic nonlinear problem.

In 2018, Pritpal Singh et al<sup>39</sup> have introduced a quantum model for time series data, which depends on the appropriate length of intervals. It is extensively employed in a financial and business forecast based on the historical pattern of data points collected over time and comparing it with the current trends. It is crippled by errors in the form of noise, faults, and loss of quantum coherence, which is crucial to their operation. In 2018, Gaurav Dhiman and Vijay Kumar<sup>40</sup> have developed an astrophysics-based approach for automatically finding the clusters and features simultaneously. It is used to solve image segmentation and microarray data analysis problems. The drawback of this approach is the randomized initial centroids selection criteria. In 2018, Gaurav Dhiman et al<sup>41</sup> have presented the ED-SHO, for solving both convex and non-convex economic dispatch problems. It can solve the economic load power dispatch problem and converge toward the optimum with low computational efforts. Moreover, the time taken for the convergence is high. In 2019, Gaurav Dhiman and Amandeep Kaur<sup>42</sup> have proposed STOA for solving constrained industrial problems. It has a high computational cost, nonlinear constraints, and a huge amount of solution spaces, and hence the approach is complicated. Therefore, solving such problems with a large number of variables and constraints is a tedious task. But, local optimum solutions do not guarantee the best solution using classical numerical methods. In 2019, Gaurav Dhiman<sup>43</sup> have developed an emperor penguin and sulp swarm algorithm (ESA) that imitates the huddling and swarm behaviors of emperor penguin optimizer and sulp swarm algorithm, respectively. The multiple solutions can share the information between each other around the search space and avoid local optimal solutions.

In 2019, Gaurav Dhiman<sup>44</sup> has developed MOSHEPO for solving both convex and non-convex economic dispatch and microgrid power dispatch problems. It is easy to update the position from other agents. It is applicable for smaller optimization problems and but, the problem persists in the algorithm while dealing with large solution space as it gets stuck in a local optimum. In 2019, Mohammad Dehghani et al<sup>45</sup> have suggested BOSA solve the optimization problems. In this, the conventional methods failed to deal with non-linear problems. The BOSA has exposure to the curse of dimensionality. In 2019, Pritpal Singh et al<sup>46</sup> have presented HOFTSM and HOFTSLPM to improve the accuracy of time series using the quantum approach. It is applicable to a small set of data and uses linguistic values instead of crisp ones. The drawback of this model is its unsuitability for complex problems. In 2020, Meenakshi Garg and Gaurav Dhiman<sup>47</sup> have introduced defect detection methods. In this, a CNN classifier is used to find the defect in an image's target area. It has numerous advantages like reduction in time and cost and helps to build the object detection classifier with high generalization potential and high detection accuracy. However, there are drawbacks of increasing computational costs and processing resources that hinder CNN's use in resource-limited environments such as mobile or embedded phones. In 2019, Dhiman, and Gaurav<sup>48</sup> have suggested MOSHO for solving real-life engineering design problems. It is used for cluster mesh vertices into the improper and proper selection to be watermark carrier based on the feature vector, with high robustness, and sensitivity. However, the algorithm cannot recover from database corruption. In 2020, Satnam Kaur et al<sup>49</sup> have proposed TSA to imitate jet propulsion and swarm behaviors of tunicates during the navigation and foraging process. It can solve multi-objective optimization problems. It requires lesser control parameters and fast convergence. It also faces a few drawbacks that could affect performance achievement such as expensive and high time consumption.

## 2.2 | Review

The treatment methods for liver tumors like surgical resection, locoregional ablation, and interventional therapy require the accurately segmented images. Moreover, these techniques require the whole tumor information such as location, shape, and size before therapy to provide fine treatment. Several approaches based on machine learning approaches were developed to segment liver tumors from CT images, which includes traditional machine learning as well as deep learning approaches. With the help of classical deep learning methods, the

image-level segmentation has resulted in undesirable sensitivity for segmenting liver tumor. Also, the challenges with the conventional methods for segmentation include high computational time, over-segmentation. In most cases, the traditional algorithm cannot determine the shade of the real image and thus produces extreme segmentation for original images. Even though there are multiple classifiers for diagnosing liver tumors, still there are some defects with the existing models so, that a new model needs to be implemented for accurate segmentation and classification. Table 1 describes the conventional liver tumor segmentation and classification techniques.

## 3 | LIVER TUMOR SEGMENTATION AND CLASSIFICATION: DEVELOPED METHODOLOGY

### 3.1 | Proposed architecture

Nowadays, liver tumor segmentation has been done manually by the radiologists on multiple CT images through slice by slice analysis. The manual approach is quite complex and consuming more time. The segmented regions are provided for the computer-aided diagnosis, and the manually segmented images may result in reduced efficiency in diagnosis. The major challenges of the automatic liver and liver tumor segmentation models are (a) brightness of the CT images among the liver tumor and the healthy tissue are low and the boundaries around the liver tumor are blurring, (b) the size, location, and shape of liver tumors are variable, thus making the segmentation difficult, and (c) liver is closely connected with the adjacent organs and these organs will hold the similar CT value as the liver. The architectural view of the proposed liver tumor segmentation and classification is shown in Figure 1.

The proposed liver tumor segmentation and classification approach include five phases such as "(a) Image pre-processing, (b) Liver segmentation, (c) Tumor segmentation, (d) Feature extraction, and (e) Classification." Initially, the CT images are gathered and the images are subjected to the pre-processing phase, in which histogram equalization and median filtering approaches are performed. The histogram equalization is employed for enhancing the contrast of the image, whereas the medial filtering is used to eliminate the unwanted noise from the image. Next to the pre-processing phase, the liver is segmented from the CT image with the help of an adaptive thresholding approach followed by level set segmentation. Once the liver is segmented from the abdominal region, the tumor segmentation is done by the Fuzzy

**TABLE 1** Features and challenges of existing liver tumor classification approaches

<b>Author (citation)</b>	<b>Methodology</b>	<b>Features</b>	<b>Challenges</b>
Dongantekin et al <sup>6</sup>	CNN	<ul style="list-style-type: none"> <li>Has better performance.</li> <li>It is one of the triumphant classifiers for image recognition.</li> </ul>	<ul style="list-style-type: none"> <li>More capacity computers are required.</li> </ul>
Anter and Hassenian <sup>24</sup>	FFCM with PSO	<ul style="list-style-type: none"> <li>It is accurate and consumes less amount of time.</li> <li>It is less sensitive to noise.</li> </ul>	<ul style="list-style-type: none"> <li>It should be validated on real time datasets.</li> <li>More theoretical analysis needs to be performed.</li> </ul>
Anter and Hassenian <sup>26</sup>	FFCM	<ul style="list-style-type: none"> <li>It is utilized for statistical data analysis.</li> <li>It is a generalization of the hard clustering approach.</li> </ul>	<ul style="list-style-type: none"> <li>Need to implement more number of CT images for validating the performance.</li> </ul>
Chang et al <sup>20</sup>	Logistic Regression	<ul style="list-style-type: none"> <li>It is employed to categorize the tumors by leave-one-out cross-validation.</li> <li>Has high performance.</li> </ul>	<ul style="list-style-type: none"> <li>Need to implement more methods for attaining tumor alignment automatically.</li> </ul>
Smeets et al <sup>19</sup>	SPPC	<ul style="list-style-type: none"> <li>It is used to compute the speed image, guiding the propagation of the level set.</li> <li>It computes the probability that a particular pixel belongs to a particular image class.</li> </ul>	<ul style="list-style-type: none"> <li>Need to improve the accuracy when considered a large number of data.</li> </ul>
Das et al <sup>21</sup>	DT	<ul style="list-style-type: none"> <li>Has an improved performance.</li> <li>It is an effective model for automatic image recognition of liver cancer.</li> </ul>	<ul style="list-style-type: none"> <li>Requires more training time.</li> </ul>
Bai et al <sup>27</sup>	3D FRN	<ul style="list-style-type: none"> <li>It consists of many shortcut connections while performing backpropagation.</li> <li>Increases speed.</li> </ul>	<ul style="list-style-type: none"> <li>Need to develop accurate segmentation methods.</li> </ul>
Chai et al <sup>28</sup>	HRMF-EM	<ul style="list-style-type: none"> <li>Reduces the computational time without influencing the accuracy.</li> <li>It enhances the classification quality acquired by EM.</li> </ul>	<ul style="list-style-type: none"> <li>It consumes more time for huge images.</li> </ul>
Kang et al <sup>29</sup>	PD-NETs	<ul style="list-style-type: none"> <li>These are heterogeneous and used in many applications.</li> <li>It shows early improvement in detecting the disease.</li> </ul>	<ul style="list-style-type: none"> <li>Performance needs to be improved.</li> </ul>
Zheng et al <sup>25</sup>	FCN	<ul style="list-style-type: none"> <li>Has attained high accuracy.</li> <li>They substitute the fully connected layer of traditional CNN with a convolutional layer and the interchanged convolutional layer restores the feature map as the actual image size.</li> </ul>	<ul style="list-style-type: none"> <li>It is very complex and it is little bit slowly.</li> </ul>
Gaurav Dhiman and Vijay Kumar <sup>28</sup>	SHO	<ul style="list-style-type: none"> <li>Faster convergence rate.</li> <li>Easy to implement.</li> </ul>	<ul style="list-style-type: none"> <li>Less computational efforts to find optimum solutions.</li> </ul>
Gaurav Dhiman, and Vijay Kumar <sup>29</sup>	EPO	<ul style="list-style-type: none"> <li>Easy to solve the constrained and unconstrained design problems.</li> </ul>	<ul style="list-style-type: none"> <li>Convergence and computational complexity are high.</li> </ul>

(Continues)

**TABLE 1** (Continued)

<b>Author (citation)</b>	<b>Methodology</b>	<b>Features</b>	<b>Challenges</b>
Gaurav Dhiman, and Vijay Kumar <sup>30</sup>	MOSHO	<ul style="list-style-type: none"> <li>Requires less time.</li> <li>High accuracy rate.</li> </ul>	<ul style="list-style-type: none"> <li>Needs improvement in overhead and detection time.</li> </ul>
Pritpal Singh and Gaurav Dhiman <sup>31</sup>	FTS	<ul style="list-style-type: none"> <li>Robust.</li> <li>Provides an approximate solution.</li> </ul>	<ul style="list-style-type: none"> <li>It affects the forecasting performance.</li> </ul>
Gaurav Dhiman, and Amandeep Kaur <sup>32</sup>	SHO	<ul style="list-style-type: none"> <li>Efficient optimizer to analyze exploration and exploitation.</li> <li>Strong global search.</li> </ul>	<ul style="list-style-type: none"> <li>Low computational efforts.</li> </ul>
Gaurav Dhiman, and Vijay Kumar <sup>33</sup>	SOA	<ul style="list-style-type: none"> <li>Can be robust.</li> <li>Short computational time.</li> </ul>	<ul style="list-style-type: none"> <li>Difficult to define initial design parameters.</li> </ul>
Gaurav Dhiman, and Vijay Kumar <sup>34</sup>	SHO	<ul style="list-style-type: none"> <li>Produce results with high accuracy.</li> <li>It generates a better quality solution and gives stable convergence.</li> </ul>	<ul style="list-style-type: none"> <li>It is not flexible</li> <li>It suffers from slow searching speed.</li> </ul>
Pritpal Singh, and Gaurav Dhiman <sup>35</sup>	RSHRSIs	<ul style="list-style-type: none"> <li>It can easily quantify the low quality pixels to high-quality pixels</li> </ul>	<ul style="list-style-type: none"> <li>Difficult to implement.</li> <li>Requires more available data.</li> </ul>
Gaurav Dhiman, and Amandeep Kaur <sup>36</sup>	HPSSHO	<ul style="list-style-type: none"> <li>Can be simple to implement.</li> <li>Have few parameters to adjust.</li> </ul>	<ul style="list-style-type: none"> <li>Cannot work out the problems of scattering.</li> </ul>
Gaurav Dhiman, and Amandeep Kaur <sup>37</sup>	SHO	<ul style="list-style-type: none"> <li>Efficient optimizer to solve the problems.</li> <li>Easy to generate the near-optimal designs.</li> </ul>	<ul style="list-style-type: none"> <li>A high initial set up cost.</li> <li>Not well at exploring the search space.</li> </ul>
Amandeep Kaur et al <sup>38</sup>	Schrodinger equation and Monte Carlo method	<ul style="list-style-type: none"> <li>Easy to solve the dynamic nonlinear problems.</li> </ul>	<ul style="list-style-type: none"> <li>Needs to improve the speed to know the best classical approach.</li> </ul>
Pritpal Singh et al <sup>39</sup>	Quantum model	<ul style="list-style-type: none"> <li>Extensively used in a financial and business forecast.</li> </ul>	<ul style="list-style-type: none"> <li>Crippled by errors in the form of noise, faults, and loss of quantum coherence.</li> </ul>
Gaurav Dhiman, and Vijay Kumar <sup>40</sup>	astrophysics-based approach	<ul style="list-style-type: none"> <li>High-speed performance.</li> <li>Ease of implementation.</li> </ul>	<ul style="list-style-type: none"> <li>Computational cost is high.</li> </ul>
Gaurav Dhiman et al <sup>41</sup>	ED-SHO	<ul style="list-style-type: none"> <li>Easy to solve convex and non-convex problem and micro grid power dispatch problem.</li> <li>Avoid local optimum problem.</li> </ul>	<ul style="list-style-type: none"> <li>The time taken for the convergence is high.</li> </ul>
Gaurav Dhiman, and Amandeep Kaur <sup>42</sup>	STOA	<ul style="list-style-type: none"> <li>High computational cost.</li> <li>A huge amount of solution spaces.</li> </ul>	<ul style="list-style-type: none"> <li>Local optimum does not guarantee the best solution using classical numerical methods.</li> </ul>
Gaurav Dhiman <sup>43</sup>	ESA	<ul style="list-style-type: none"> <li>The exploration capability of multiple-solution or population-based metaheuristics is better than the single solution-based metaheuristics.</li> </ul>	<ul style="list-style-type: none"> <li>It is less susceptible to scalability as compared to other algorithms.</li> </ul>
Gaurav Dhiman <sup>44</sup>	MOSHEPO	<ul style="list-style-type: none"> <li>Low computational efforts.</li> <li>Easy to update the position from other agents.</li> </ul>	<ul style="list-style-type: none"> <li>It may stuck in local optimum problems.</li> </ul>
Mohammad Dehghani et al <sup>45</sup>	BOSA	<ul style="list-style-type: none"> <li>It has a high ability to solve optimization problems.</li> </ul>	<ul style="list-style-type: none"> <li>Low flexibility.</li> <li>Less accurate.</li> </ul>

**TABLE 1** (Continued)

Author (citation)	Methodology	Features	Challenges
Pritpal Singh et al <sup>46</sup>	HOFTSM and HOFTSLPM	<ul style="list-style-type: none"> <li>More capability in a nonlinear relationship.</li> <li>Can deal with incomplete and deficient data under unclear circumstances.</li> </ul>	<ul style="list-style-type: none"> <li>Unsuitability for complex problems.</li> </ul>
Meenakshi Garg, and Gaurav Dhiman <sup>47</sup>	Defect detection method	<ul style="list-style-type: none"> <li>Reduction in time and cost.</li> <li>Easy to build the object detection classifier with high generalization potential and high detection accuracy.</li> </ul>	<ul style="list-style-type: none"> <li>Increases computational costs and processing resources.</li> </ul>
Dhiman, and Gaurav <sup>48</sup>	MOSHO	<ul style="list-style-type: none"> <li>Robustness</li> <li>Sensitivity</li> </ul>	<ul style="list-style-type: none"> <li>Inability to recover from database corruption.</li> </ul>
Satnam Kaur et al <sup>49</sup>	TSA	<ul style="list-style-type: none"> <li>Less control parameters.</li> <li>Fast convergence.</li> </ul>	<ul style="list-style-type: none"> <li>Expensive and high time consumption.</li> </ul>

centroid-based optimized region growing algorithm. As a novel contribution to the tumor segmentation, the seed point of region growing is selected by the FCM, and the tolerance or the threshold function of region growing is optimized by the improved meta-heuristic algorithms termed as O-SHO. The tolerance optimization is done in such a way that the maximum segmentation accuracy has to be obtained while compared with the ground truth image. Further, from the tumor segmented image, the features such as GLCM, shape features, and LBP are extracted. Later, these features are provided for classification, which is done by the combination of two deep learning models like CNN and RNN. Here, the tumor segmented image is given as input to the CNN, and the features extracted from the tumor region are subjected to RNN. Along with the improved segmentation, the classification is also enhanced by optimizing the number of hidden neurons of both CNN and RNN using the same proposed O-SHO. The main intent of optimizing the number of hidden neurons of both CNN and RNN is to maximize the classification accuracy. Finally, the classification results give the information in the form of two classes: one indicates that the region belongs to normal, and the other one indicates that the region belongs to the abnormal.

### 3.2 | Image description

Assume  $In^{im}$  be the input CT liver image for segmentation and classification. After pre-processing, the histogram equalized image is denoted as  $In^{HE}$ , and the noise removed image by median filtering is represented as  $In^{MF}$ . Similarly, during liver segmentation, the segmented image by adaptive thresholding is represented as  $In^{AT}$ .

and the segmented image by level set algorithm is denoted as  $In^{LS}$ . Moreover, the tumor segmented image by Fuzzy centroid-based optimized region growing algorithm is denoted as  $In^{FZ}$ . The combined features with LBP, GLCM, and shape features are extracted, and it is represented as  $FTS_k$  in which  $k = 1, 2, \dots, N_{fs}$  and the total number of features are indicated by  $fts$ .

### 3.3 | Image pre-processing

For the input CT abdominal image, the image pre-processing is performed by histogram equalization and median filtering approach.

(a) Histogram Equalization<sup>50</sup>: It is employed for pre-processing as it modifies the intensity of an image to improve the contrast of the image. Let  $In^{im}$  be the input image with  $j_R \times j_S$  matrix of integer pixel intensities lying between 0 and 1, and the count of possible intensity values are denoted as  $INV$ , generally having the maximum value as 256. The normalized histogram  $NHS$  of  $In^{HE}$  with a bin to possible intensity is denoted in Equation (1). Here, the term  $he = 0, 1, \dots, INV - 1$ . The histogram equalized image is denoted in Equation (2).

$$NHS = \frac{\text{number of pixels with density } he}{\text{total number of pixels}} \quad (1)$$

$$In^{HE} = \text{floor} \left( (INV - 1) \sum_{he=0}^{In^{im}(i,j)} NHS \right) \quad (2)$$

In the above equation, the term  $\text{floor}()$  rounds down to the nearer integer value. Therefore, the histogram

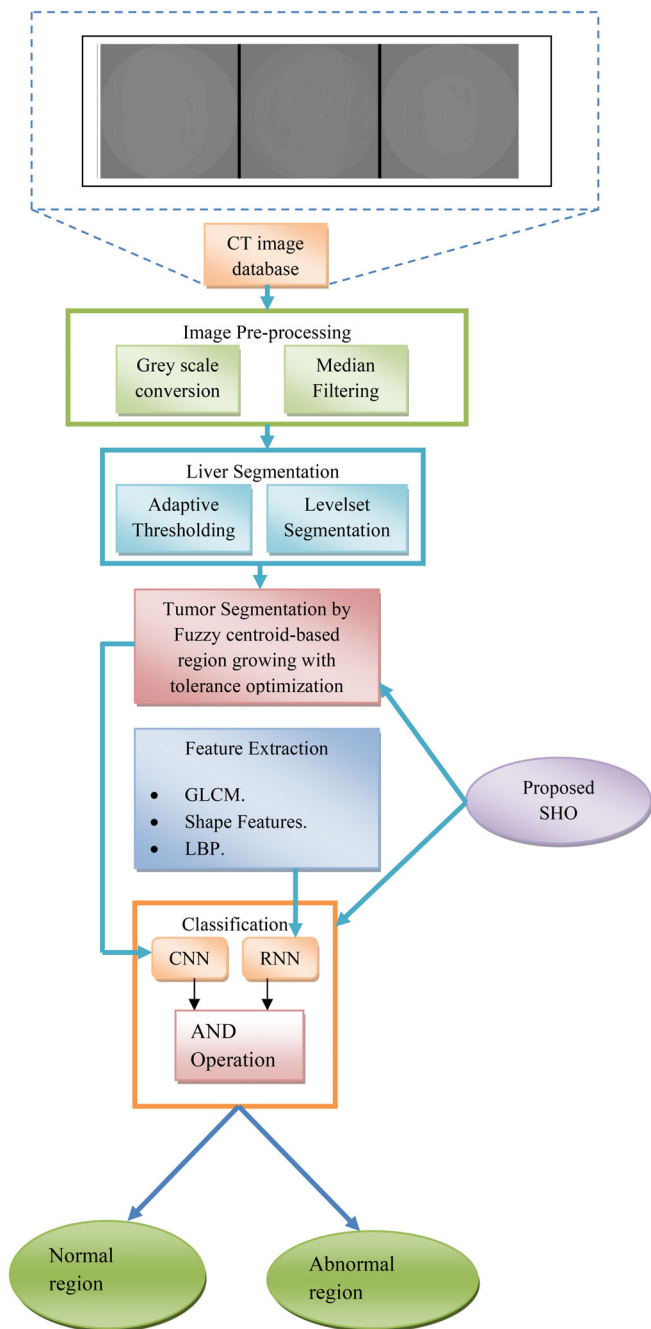


**FIGURE 1** Block diagram of liver tumor segmentation and classification [Color figure can be viewed at [wileyonlinelibrary.com](http://wileyonlinelibrary.com)]

equalized image  $In^{HE}$  is further subjected to a median filter for noise removal.

(c) Median Filtering<sup>51</sup>: This filter is used to eliminate the noise from an image by restraining the pixels of low or high frequencies, and hence will enhance or detect the image edges. The median filtering approach, which is a non-linear filter, is employed for removing the noise from

the liver image. The key objective of this filter is to substitute the noisy pixels by the median value of the surrounding pixels, which are sorted based on the image's gray level. The result  $In^{MF}$  is given based on Equation (3) when the median filter is implemented for the input image  $In^{HE}$ .

$$In^{MF}(x,y) = \text{med}\{In^{HE}(x-u,y-v) | u,v \in H\} \quad (3)$$

In Equation (3), the original and the median filtered image is denoted as  $In^{HE}$  and  $In^{MF}$ , respectively. Moreover, a 2-dimensional mask is indicated by  $H$ . Therefore, the final pre-processed image is denoted as  $In^{MF}$ , which is further subjected to liver segmentation.

### 3.4 | Liver segmentation

The liver segmentation is performed by adaptive thresholding and level set segmentation and the description of each methodology is given below.

#### 3.4.1 | Adaptive thresholding

It is selected based on a few image characteristics and hence named adaptive thresholding.<sup>52</sup> The method selects the pixel if the threshold value of the particular pixel is distinct to the discrete images. Moreover, a general technique employed for choosing the threshold value is by evaluating the image's histograms. The adaptive thresholding consists of a weight update unit to find the suitable threshold value for the bimodal images. Assume  $[M \times N]$  as the size of the image, at first, the terms  $\mu_1$  and  $\mu_2$  are the two allotted weights then these weights are contrasted with the values of each pixel in the  $[M \times N]$  image. The nearest weight is chosen to update the weight of each input pixel. The variance among the nearest weight and the input pixel is multiplied by the learning rate  $\beta$  and the added to the nearest weight. The term  $\mu_1$  is updated when  $\mu_1$  is nearer to that pixel value, whereas the term  $\mu_2$  is updated when  $\mu_2$  is very closer to that pixel value. This can be represented by using the mathematical formula given in Equation (4).

$$\mu_{\text{new}} = \mu_{\text{old}} + \beta * (\text{pixel} - \mu_{\text{old}}) \quad (4)$$

In Equation (4), the weight is indicated by  $\mu$  and the learning rate is denoted as  $\beta$ , whereas  $\beta = \frac{256 - px}{256}$ . Consequently, the updated weights are further subjected to

image pixel and at last, the averages of these two weights are considered as the threshold value and it is shown in Equation (5).

$$In^{AT} = \frac{\mu_1 + \mu_2}{2} \quad (5)$$

The image can be converted to binary form with the help of a threshold value. The pixel range below  $In^{AT}$  value is considered as background, whereas the pixel range above  $In^{AT}$  value is considered as an object, and thus the object can be discriminated easily.

### 3.4.2 | Level set segmentation

In image processing, the usage of several PDEs is relied upon the surfaces and moving curves with curvature-based velocities.<sup>53</sup> Here, the level set segmentation is very powerful and helpful in segmenting the images. The main intuition is to denote the surfaces or curves as zero level set of more dimensional hyper-surface. The level set segmentation approach not only produces accurate numerical applications but also holds the topological alterations easily. The definition for the smoothing function of the surface is denoted as  $\varphi(x, y, t)$ , whereas the definitions set for the curves are denoted as  $\varphi(x, y, t) = 0$ . Therefore, the development of the curve is transferred into the development of a three-dimensional level set function. Consider a level set function  $\varphi(x, y, t = 0)$ , whose zero level set represents the curve. The entire surface is split into external and internal regions of the curve by considering the curve as the boundary. The SDF on the surface is given by Equation (6). Here, the shortest distance among the point of  $x$  on the surface and the curve is denoted as  $sd$ .

$$\varphi(x, y, t) = 0 = sd \quad (6)$$

In the entire developmental procedure of the curve, its points are suitable for the equation represented in Equation (7). Also, Equation (8) denotes the common movement equation of level set, in which the speed function is represented as  $SF$ . The term  $SF$  is a function associated with the development of image and surface characteristics. The resultant development of the level set function is the gradient flow, and it minimizes the whole energy functional and the corresponding energy function of the level set is denoted in Equation (9).

$$\varphi(x, y, t) = 0 \quad (7)$$

$$\varphi_t SF |\Delta \varphi| = 0 \quad (8)$$

$$Eng(\varphi) = \mu Int(\varphi) + \epsilon_{ed\lambda,o}(\varphi) = \mu \int_{\Omega} \frac{1}{2} (|\Delta \varphi| - 1)^2 dx dy + \lambda \int_{\Omega} ed\delta(\varphi) |\Delta \varphi| dx dy + o \int_{\Omega} edW(\varphi) dx dy \quad (9)$$

In the above equation, the internal and external energy terms are denoted by  $Int(\varphi)$  and  $\epsilon(\varphi)$ , respectively. Moreover, the term  $\mu > 0$  denotes the parameter holding the effect of penalizing the deviation of  $\varphi$  from SDF, and the edge indicator function  $ed$  is given by Equation (10)

$$ed = \frac{1}{1 + |\Delta GS_{\sigma} * In^{AT}|^2} \quad (10)$$

In Equation (10), the image is denoted as  $In^{AT}$  and the Gaussian kernel with SD  $\sigma$  is given by  $GS_{\sigma}$ . Finally, the level set segmented image is denoted as  $In^{LS}$  and it is further subjected to tumor segmentation.

## 4 | TUMOR SEGMENTATION AND FEATURE EXTRACTION TECHNIQUES USED FOR EFFECTIVE TRAINING

### 4.1 | Fuzzy centroid-based optimized region growing for segmentation

To segment the tumor from the liver part, the Fuzzy centroid-based optimized region growing method is used in the final  $In^{LS}$  image. This is the modified version of the single seeded region growing algorithm.<sup>54</sup> In present times, the seeded region growing model is employed for various types of tumor segmentation. This model works based on the objective of clustering the target pixels into significant image regions. In the traditional region growing methods, the functions with seed are chosen at random, which may result in performance degradation. As an improvement, the advantageous notion of FCM is employed in this article for choosing the seed point. In this work, the FCM-based clustering centroid is used for selecting the starting seed point for performing the region growing algorithm. FCM<sup>55</sup> is an iterative clustering method that offers an optimal  $w$  portion of the dataset by minimizing the weighted function in the cluster sum of the squared error energy function, and the corresponding formula for the FCM is denoted in Equation (11).

$$FCM_{\min} = \sum_{p=1}^N \sum_{q=1}^w m s_{pq}^{\min} sqd^2(X_p, Y_q) \quad (11)$$

In the above equation, the degree of membership of  $X_p$  in  $q^{th}$  cluster is denoted as  $m s_{pq}^{\min}$ , the weighting exponent on each fuzzy membership is denoted as min, where  $\min \geq 2$ . The term  $Y_q$  is the centroid, which is assigned as the starting seed point of the region growing algorithm.

The image segmentation in the region growing model is capable of using a seed pixel and later links the new homogenous pixels to the seed until the segmentation scenario is contented on the inflated segment. Assume, the entire region  $J$  of the input image  $In^{pre}$  is split into  $z$  sub-regions  $J_1, J_2, \dots, J_z$ . The below-mentioned limitations should be satisfied in the region growing model for the effective segmentation of the images.

$$\cup_{U=1}^w J_U = J;$$

1. The associated region is denoted as  $J_1, J_2, \dots, J_w$ ;
2. To any  $U, V, U \neq V, J_U \cap J_V = \emptyset$ ;

$$P(J_U) = true;$$

$$J(J_U \cup J_V) = false;$$

In this region growing model, the gray level value of the set  $J_U$  is denoted as  $P(J_U)$ , the overall sum of the image pixels is denoted as  $os$ . In the initial stage, the seed point is collected as the prime procedure. For the above given set, the sum of an individual pixel is included by each of the models when the pixel values consist of the statement shown in Equation (12), and Equation (13) is obtained.

$$avg = \frac{1}{os} \sum_{(i,j) \in J} Fe(i,j) \quad (12)$$

$$|Fe(i,j) - avg|_{(i,j) \in J} < \delta \quad (13)$$

In the above equations, the term  $avg$  denotes the mean of the image, the term  $Fe(i, j)$  indicates the coordinates of  $(i, j)$ , and the threshold is indicated by  $\delta$ , which is very close to the mean of an image. The operation of the Fuzzy centroid-based optimized region growing by proposed O-SHO is shown in Figure 2.

According to the functioning theory of the region growing model, the selection of seed points plays a

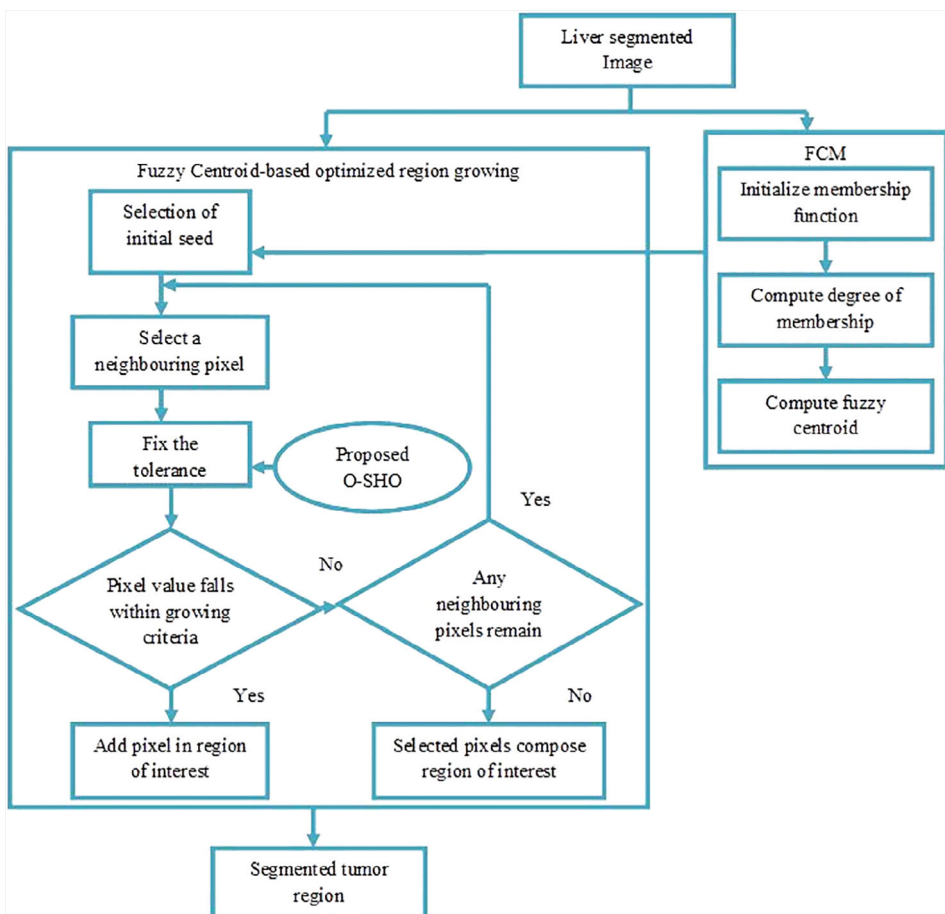


**FIGURE 2** Liver tumor segmentation by Fuzzy centroid-based optimized region growing [Color figure can be viewed at [wileyonlinelibrary.com](http://wileyonlinelibrary.com)].

major role in enhancing the segmentation performance. The conventional seeded region growing method needs more human effort for selecting the seed point at random, and this disadvantage is improved by using the FCM clustering centroid for the seed selection. Also, the tolerance or threshold function  $\delta$  is optimized by the proposed O-SHO to attain better segmentation. Thus, the segmented image  $In^{FZ}$  is obtained after tumor segmentation, which is further subjected to feature extraction for extracting the features for the classification task.

## 4.2 | Feature extraction

For performing the feature extraction, GLCM and LBP are extracted and the descriptions of each methodology are given below.

### 4.2.1 | GLCM

This method is used to compute the texture features by taking the spatial association of pixels into consideration. Also, it is utilized for analyzing the probability of pixels pairs by specific values, which helps to examine the spatial relationship of pixels in an image. The mathematical equation for energy is indicated by Equation (14). Here, the  $(g, h)^{th}$  element in the normalized GLCM is indicated by  $E_{gh}$ .

$$EGY = \sum_g \sum_h E_{gh}^2 \quad (14)$$

The mathematical equation for contrast, entropy, and homogeneity is expressed in Equation (15), Equation (16), and Equation (17), respectively.

$$CST = \sum_g \sum_h (g-h)^2 E_{gh} \quad (15)$$

$$EPY = - \sum_g \sum_h E_{gh} \log_2 E_{gh} \quad (16)$$

$$HGY = \sum_g \sum_h \frac{1}{1 + (g-h)^2} E_{gh} \quad (17)$$

Also, the sum average, correlation, and variance are denoted in Equation (18), Equation (19), and Equation (20), respectively. Here,  $E_k$  and  $E_l$  indicates  $k^{th}$  and  $l^{th}$  coordinate in GLCM element.

$$SUA = \sum_{g=2}^{2N_G-2} g E_{k+l}(g) \quad (18)$$

$$CRL = \frac{\sum_g \sum_h (g \times h) E_{gh} - \mu_g \mu_h}{\sigma_g \sigma_h} \quad (19)$$

$$VRN = \sum_g \sum_h (g - \mu)^2 E_{gh} \quad (20)$$

In the above equations, the mean  $E_{gh}$  is denoted as  $\mu$  and the number of gray levels in the image is denoted as  $N_G$ . The mean of  $E_g$  and  $E_h$  is denoted as  $\mu_g$  and  $\mu_h$ , and the SD of  $E_g$  and  $E_h$  is denoted as  $\sigma_g$  and  $\sigma_h$ . Also, “the sum entropy, sum variance, difference entropy, difference variance, information metrics of correlation, and maximum correlation coefficient” are denoted in Equations (21) to (26), respectively.

$$SET = \sum_{g=2}^{2N_G} E_{k+l}(g) \log \{E_{k+l}(g)\} \quad (21)$$

$$SVR = \sum_{g=2}^{2N_G} (g - SUA)^2 E_{k+l}(g) \quad (22)$$

$$DET = \sum_{g=0}^{N_G-1} E_{k-l}(g) \log \{E_{k-l}(g)\} \quad (23)$$

$$DVR = \text{Variance of } E_{k-l} \quad (24)$$

$$IMC1 = \frac{EPQ - EPQ1}{\max\{EP, EQ\}} \quad (25)$$

Here,  $EP$  and  $EQ$  are the entropies of  $E_k$  and  $E_l$ .

$$IMC2 = \sqrt{(1 - \exp[-2.0[EPQ2 - EPQ]])} \quad (26)$$

In Equations (25) and (26), the terms  $EPQ$ ,  $EPQ1$ , and  $EPQ2$  are represented in Equation (27), Equation (28), and Equation (29), respectively.

$$EPQ = - \sum_g \sum_h E_{gh} \log_2 E_{gh} \quad (27)$$

$$EPQ1 = - \sum_g \sum_h E_{gh} \log_2 \{E_k(g) E_l(h)\} \quad (28)$$

$$EPQ2 = - \sum_g \sum_h E_k(g) E_l(h) \log_2 \{E_k(g) E_l(h)\} \quad (29)$$

The numerical equation for MCC is denoted in Equation (30).

$$MCC = \sum_e \frac{E(g,e)E(h,e)}{E_k(g)E_l(e)} \quad (30)$$

#### 4.2.2 | Shape features

The shape features including area, perimeter, and label connected components are extracted from the segmented image.

##### *Area*

“The area feature estimates the area of the objects in the binary image” and its equation is denoted in Equation (31). Here, the binary image is denoted as *bw* and the term *Tot* denotes “the scalar value which corresponds roughly to the total number of pixels in the image, but the value might not be the same because different patterns of pixels are weighted differently”

$$Tot = bwarea(bw) \quad (31)$$

##### *Perimeter*

“It returns a binary image that contains only the perimeter pixels of objects in the input image. A pixel is part of the perimeter if it is nonzero and it is connected to at least one zero-valued pixel.” The mathematical equation is denoted in Equations (32) and (33). In Equation (33), the term *conn* specifies the pixel connectivity.

$$bw2 = bwperim(bw) \quad (32)$$

$$bw2 = bwperim(bw, conn) \quad (33)$$

##### *Label connected components*

“It returns the label matrix *Lb*, which contains labels for the 8-connected objects found in *bw*. The numerical formula is shown in Equations (34) and (35), in which the pixel connectivity is denoted as *conn*.

$$Lb = bwlabel(bw) \quad (34)$$

$$Lb = bwlabel(bw, conn) \quad (35)$$

It is suggested as a robust and effective texture description that could be developed in broad applications from texture segmentation to image recognition.<sup>56</sup> Each pixel's neighborhood is threshold by the middle value, thus the LBP operator classifies the pixel of an image and the result is considered as the binary value. The histogram of the classes is computed and used as a texture descriptor if each pixel is classified according to LBP codes. The labeled image's histogram  $In^{FZ}(x, y)$  is used as a descriptor and the corresponding equation is denoted in Equation (36).

$$Hgm_{im} = \sum_{x,y} I(In^{FZ}(x,y) = im), im = 0, \dots, e-1 \quad (36)$$

#### 4.2.3 | LBP

In the above equation, the term *e* refers to the count of different labels given by the LBP operator. If *C* is false, then  $I(C) = 0$  otherwise  $I(C) = 1$ . Also, a circular neighborhood is considered around the pixel. The points *Ps* are chosen with a radius *Rd* on the circle's circumference. By considering  $LBP_{Ps,Rd}$  as *Ps*-bit binary number  $(r_{Ps-1}, r_{Ps-2}, \dots, r_1, r_0)$ , the uniformity metric (*UF*) is defined by Equation (37) to get a rotation-invariant uniform pattern with finer angular quantization. The rotation invariant uniform pattern value less than or equal to 2 is shown in Equation (38).

$$UF(LBP_{Ps,Rd}) = |r_{Ps-1} - r_0| + \sum_{Ps=1}^{Ps-1} |r_{Ps} - r_{Ps-1}| \quad (37)$$

$$LBP_{Ps,Rd} = \begin{cases} \sum_{ps=0}^{Ps-1} s(gr_{ps} - gr_{cp}) & \text{if } UF(LBP_{Ps,Rd}) \leq 2 \\ Ps + 1 & \text{Otherwise} \end{cases} \quad (38)$$

In the above equation, the term  $gr_{cp}$  denotes the gray value of the center pixel, and the gray values of *Ps* points are denoted as  $gr_{ps}$ ,  $ps = 0, \dots, Ps - 1$ . By choosing the circles with a different radius around the center pixels, a multi-scale assessment is performed by LBP and generates a different LBP image to each scale. Also, the entropy and energy of the LBP image are constructed over distinct scales  $Rd = 1, 2, \text{ and } 3$  by the corresponding pixel count  $Ps = 8, 16, \text{ and } 24$  as the feature descriptor.

Finally, all three sets of features are combined, and it is represented as  $FTS_k$  and these are applied to a classifier, in which  $k = 1, 2, \dots, N_{fts}$  and the total number of

features are indicated by  $N_{fts} = 55$ , where the features of GLCM, Shape features, and LBP are 46, 5, and 4, respectively.

## 5 | IMPROVED SPOTTED HYENA OPTIMIZATION FOR ENHANCING THE HYBRID CLASSIFIER

### 5.1 | Conventional spotted hyena optimization algorithm

The inspiration for the traditional SHO<sup>18</sup> comes from the hunting behavior of spotted hyenas. The associations of these hyenas are dynamic in nature. There are three basic phases in the optimization procedure of traditional SHO like searching for the prey, encircling the prey, and attacking the prey. With the location of the prey, these hyenas are well-known and encircle them. The current best solution is taken into consideration as the target for the mathematical representation of the hyenas. The other search agents strive for updating their respective solutions after determining the best search candidate solution, and the corresponding equation is expressed in Equation (39). The position vector of the spotted hyena is indicated in Equation (40).

$$D_{hn} = |A \cdot PV_{py}(It) - PV(It)| \quad (39)$$

$$PV(It + 1) = PV_{py}(It) - B \cdot D_{hn} \quad (40)$$

In the above equations, the distance among the prey and the spotted hyena is indicated by  $D_{hn}$ . The coefficient vectors are denoted as  $A$  and  $B$ . The position vector of the spotted hyena and the prey is represented as  $PV$  and  $PV_{py}$ , respectively. The coefficient vectors are expressed in Equations (41) and (42). Here, the term  $a$  is represented in Equation (43). In Equation (43), the term  $a$  is reduced from 5 to 0 in a certain period for the maximum number of iterations. Moreover, the random vectors are indicated by  $ran_1$  and  $ran_2$  ranging from 0 to 1. With the help of Equations (39) and (40), the location of the spotted hyena is updated randomly around the prey.

$$A = 2 \cdot ran_1 \quad (41)$$

$$B = 2a \cdot ran_2 - a \quad (42)$$

$$a = 5 - \left( iter * \left( \frac{5}{\max_{iter}} \right) \right) \quad (43)$$

The best search agent is taken into consideration for defining the spotted hyena's behavior; whichever is optimum has the information related to the location of the prey. The hunting behavior of spotted hyenas is denoted in Equations (44), (45), and (46).

$$D_{hn} = |K \cdot PV_{hn} - PV_{lr}| \quad (44)$$

$$PV_{lr} = PV_{hn} - B \cdot D_{hn} \quad (45)$$

$$Cl_{shn} = PV_{lr} + PV_{lr+1} + \dots + PV_{lr+GN} \quad (46)$$

In the above-mentioned equations, the position of the best spotted hyena is indicated by  $PV_{hn}$  and the positions of the other spotted hyenas are indicated by  $PV_{lr}$ . In the group of  $GN$  number of optimal solutions is represented as  $Cl_{shn}$  and the total number of spotted hyenas is denoted as  $N$  and the mathematical equation is expressed in Equation (47).

$$GN = Co_{nos}(PV_{hn}, PV_{hn+1}, \dots, (PV_{hn} + rnv)) \quad (47)$$

In the above equations, the total number of solutions is indicated by  $nos$  and the count of all the candidate solutions is denoted as  $Co_{nos}$ . The term  $rnv$  is the random vector lies between 0.5 and 1. The value of the vector  $a$  is decreased to model the attacking of prey. The variance in the vector  $B$  is also decreased to change the value of vector  $a$ , and its value is reduced from 5 to 0 for a certain period of iterations. The attacking of prey is given in Equation (48).

$$PV(It + 1) = \frac{Cl_{shn}}{GN} \quad (48)$$

In Equation (48), the term  $PV(It + 1)$  saves the best solution and updates the location of remaining search agents based on the position of the best search agent. Based on the location of spotted hyenas set, which are present in the vector  $Cl_{shn}$ , they mostly search for the prey in this way. Also, the hyenas move away from each other to search for the prey and attack it. The algorithmic representation of the conventional spotted hyena is shown in Algorithm 1.

**Algorithm 1: Pseudocode of conventional SHO<sup>18</sup>**

**Input:** Perform population initialization as  $PV_i$ , where  $i = 1, 2, \dots, ne$

**Output:** Best solution

Do parameter initialization  $a, A, B, GN$

Perform the fitness evaluation

$PV_{hn}$  is the best search agent

$Cl_{shn}$  indicates the group of all far optimal solutions

**while** ( $It < It_{max}$ )

- for each** search agent
- Update the solution by Equation (48)
- end for**
- $a, A, B, GN$  are updated
- Check the search space of each search agent
- Evaluate the fitness value of each search agent
- Update  $PV_{hn}$  if a better solution occurs than the previous one.
- Update the group  $Cl_{shn}$  with respect to  $PV_{hn}$
- $It = It + 1$

**end while**

**return**  $PV_{hn}$

## 5.2 | Proposed O-SHO

The main benefit of the conventional SHO algorithm is its efficiency in the exploration stage on multi-modal functions for obtaining the best convergence in all the iterations. Along with that, the classical optimization algorithm has its best performance of the exploration stage while testing the uni-modal functions. However, there are few disadvantages such as unsuitable for solving optimization issues, and the convergence speed is very less. To further improvise the performance of existing SHO in segmentation and classification, an improved version termed as O-SHO is introduced. The proposed O-SHO works based on the “trail checking approach,” which solves the problem of convergence speed related to the conventional SHO. The trial is incremented as 1 if there is no improvement with the solution in the current iteration than the previous iteration. If  $trial < 5$ , the solution is updated based on the Equation (48) concerning the best solution. On the other hand, the solution is updated by Equation (49) concerning the worst position  $PV_{hn(worst)}$  for the condition  $trial \geq 5$ . As the algorithm considers the worst solution along with the best solution,

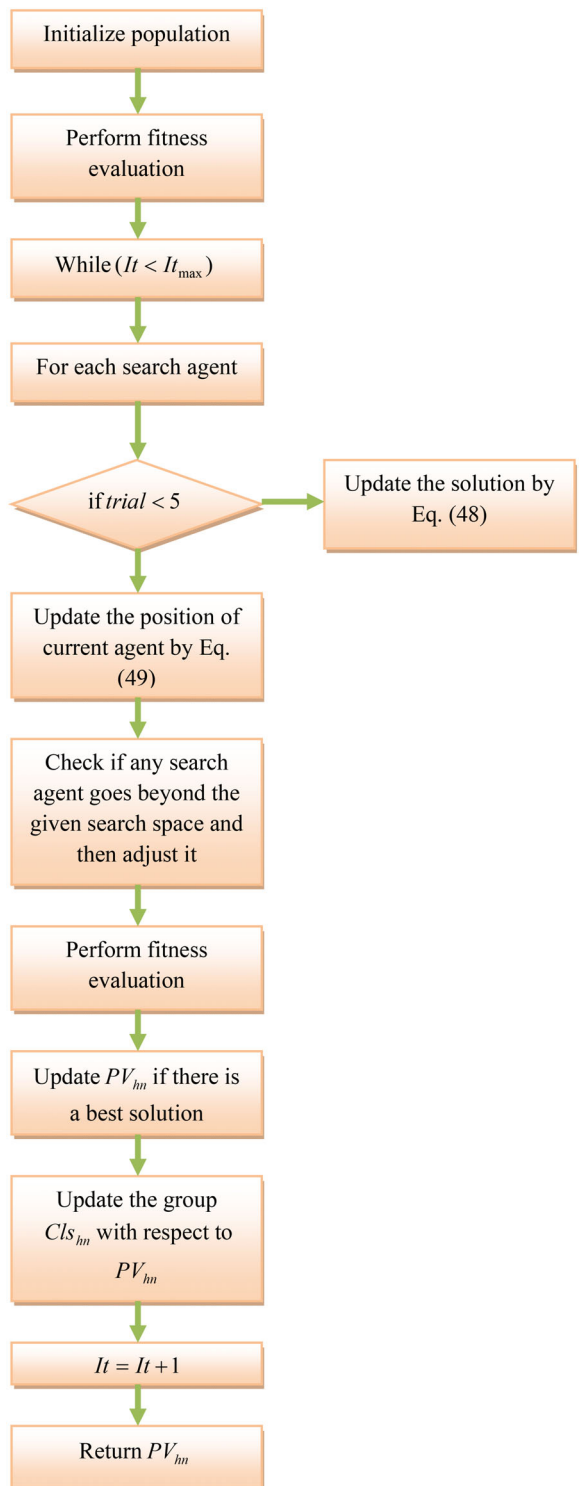


**FIGURE 3** Flowchart of proposed O-SHO for segmentation and classification. O-SHO, opposition-based spotted hyena optimization [Color figure can be viewed at wileyonlinelibrary.com]

it is termed as an opposition-based algorithm. The pseudo-code of the proposed O-SHO is shown in Figure 3.

$$PV_{lr} = PV_{hn(worst)} - B \cdot D_{hn} \quad (49)$$

Among various improvements in the past researches, opposition-based alterations have received great attention. Moreover, opposition based solution variables have intended for driving not only in the direction of better solutions but also outwards poor solution. Opposition-based optimization principles use search space for determining the initial solution variables. Opposition-based optimization has been observed as a promising outcome in earlier researches.<sup>57</sup>

#### Algorithm 2: Pseudocode of proposed O-SHO

```

Input: Perform population initialization as  $PV_i$ , where  $i = 1, 2, \dots, ne$ 
Output: Best solution
Do parameter initialization  $a, A, B, GN$ 
Perform the fitness evaluation
 $PV_{hn}$  is the best search agent
 $Cl_{hn}$  indicates the group of all far optimal solutions
while ( $It < It_{max}$ )
  for each search agent
    Check trial—>improvement
    If  $trial < 5$ 
      Update the solution by Equation (48)
    Else if  $trial \geq 5$ 
      Update the solution by Equation (49)
    End if
  end for
   $a, A, B, GN$  are updated
  Check the search space of each search agent
  Evaluate the fitness value of each search agent
  Update  $PV_{hn}$  if a better solution occurs than the previous one
  Update the group  $Cl_{hn}$  with respect to  $PV_{hn}$ 
   $It = It + 1$ 
end while
return  $PV_{hn}$ 

```

### 5.3 | Objective model

The proposed research work focuses on optimized segmentation and classification. The segmentation of liver tumors is performed by the Fuzzy centroid-based optimized region growing. Here, the tolerance of region growing is optimized by the proposed O-SHO algorithm. The main objective of the optimized region growing is to maximize the

segmentation accuracy concerning the ground truth image. Also, the hybrid classifier is developed by combining the RNN and CNN techniques and its performance is improved by optimizing the number of hidden neurons by the proposed O-SHO algorithm. The objective model is defined as maximizing the classification accuracy.

The mathematical equation for accuracy is denoted in Equation (50), in which the true positives and negatives are denoted as  $T_p$  and  $T_n$ , respectively. Moreover, the false positives and false negatives are represented as  $F_p$  and  $F_n$ , respectively.

$$Acc = \frac{T_p + T_n}{T_p + T_n + F_p + F_n} \quad (50)$$

The maximization of accuracy for segmentation and classification is done by the proposed O-SHO algorithm, and the objective model is given in Equation (51)

$$obj = \arg \min_{\{\delta, hdn_{CNN}, hdn_{RNN}\}} \quad (51)$$

Here,  $\delta$  indicates the tolerance of region growing algorithm,  $hdn_{CNN}$  and  $hdn_{RNN}$  indicate the number of hidden neurons of both CNN and RNN, respectively.

### 5.4 | Solution encoding

In the segmentation phase, the threshold function of the region growing algorithm is optimized by the developed O-SHO. The solution encoding of the optimized segmentation is shown in Figure 4. The range of tolerance is between (0,1).



**Threshold  
function**

**FIGURE 4** Solution encoding for optimized region growing-based segmentation [Color figure can be viewed at [wileyonlinelibrary.com](https://wileyonlinelibrary.com)]

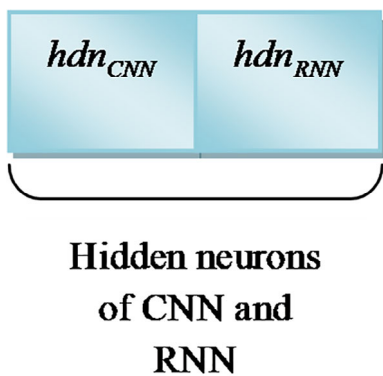


**FIGURE 5** Solution encoding for optimized hybrid classifier [Color figure can be viewed at [wileyonlinelibrary.com](http://wileyonlinelibrary.com)]

Moreover, the solution encoding of an optimized hybrid classification is shown in Figure 5, in which the number of hidden neurons is chosen in the range between (5, 20).

## 5.5 | Convolutional neural network

CNN takes the tumor segmented image resulted from the proposed segmentation scheme as input. This network<sup>58</sup> is a feed forward network, where the information flows only in one direction, which is from input to output and is inspired by ANNs. CNN consists of various layers like pooling and convolutional layers, which are combined to form modules. Also, either one or more fully connected layers similar to feed forward NNs follow these modules. The input image is directly transferred to the network and this is applied for several stages of pooling and convolutional layers. The final fully connected layer resultant is shown using the class labels. The descriptions for each layer of CNN are as follows.

### 5.5.1 | Convolutional layers

It is used by the feature extractors and the layers evaluate the feature depictions of the input image. The neurons existing in these layers are arranged into feature maps. Each neuron in the feature map includes a receptive field, which is associated with the surrounding neurons existing in the past layer with a set of trainable weights and the filter bank.

### 5.5.2 | Pooling layers

The utilization of these layers is to decrease the spatial resolution of feature maps, and these layers are used to

obtain spatial invariance to input distortions and translations. Every resultant map might combine convolution with several input maps and the corresponding equation is indicated by Equation (52). Here, the convolutional layer is indicated by  $cl$ , and the down sampling layer is denoted as  $cl - 1$ . The input features of the down sampling layer are denoted as  $Frs^{cl-1}$ , and the kernel map is denoted as  $Kr_{cd}^{cl}$ . Moreover, the additive bias of the convolutional layer is indicated by  $Abb_d^{cl}$  and the term  $IN_d$ . The input and output are denoted as  $c$  and  $d$ , respectively.

$$Frs_{bcd}^{cl} = f \left( \sum_{c \in IN_d} Frs_c^{cl-1} * Kr_{cd}^{cl} + Abb_d^{cl} \right) \quad (52)$$

In each region, max-pooling selects the key element, in which the result of the pooling function is associated using  $b^{th}$  feature map, is denoted as  $Frs_{bcd}^{cl}$ .

### 5.5.3 | Fully connected layers

Numerous convolutional and pooling layers are usually placed on top of each other for extracting the best abstract feature representations in the network. These layers follow fully connected layers to learn the feature representations and finally the high-level reasoning function is done in the fully connected layers to classify the segmented image.

### 5.5.4 | Training

Generally, CNNs and ANNs employ learning models to change the free parameters for acquiring the required output of the network. Backpropagation is the important method employed for the training of the CNN classifier.

## 5.6 | Recurrent neural network

The RNN takes the combined features extracted from the tumor segmented image as input. This network<sup>59</sup> is one kind of ANN, where the links among the nodes create a directed graph with the help of progression information. RNN can work with time-series data effectively, and therefore the result of RNN is found to be the best one when regulating the previous and the present data. Moreover, it consists of LSTM that includes input, forget, and output gates. It is used to resolve the gradient explosion and mass. Also, LSTM removes the unnecessary data and acquires the required information when the state of the memory cell unit is updated with three gates. GRU is introduced as the type of LSTM, in which it is used to

build RNN for enhancing the performance. It combines output and forget gates into a single update gate  $ug_b$ . Here, the linear interpolation assists to acquire the current result. Consider  $F_b \leftarrow FTS_k$  as the  $b^{th}$  input feature, and the past hidden state is indicated by  $hdn_{b-1}$ . The update and reset gate is shown in Equation (53) and Equation (54), respectively. Here, the activation function is denoted as  $avf$ , which is the logistic sigmoid function.

$$ug_b = avf(wt^{Fug}F_b + wt^{Gug}G_{b-1}) \quad (53)$$

$$rg_b = avf(wt^{Frg}F_b + wt^{Grg}G_{b-1}) \quad (54)$$

The weight matrix is denoted as  $wt^b = \{wt^{Fug}, wt^{Gug}, wt^{Frg}, wt^{Grg}\}$ . The candidate state of the hidden unit is measured using Equation (55), in which the element-wise product is denoted as  $\oplus$ . The linear interpolation is denoted as  $G_{b-1}$  and the candidate state is denoted as  $\tilde{G}_b$ , and the hidden state as  $b^{th}$  hidden activation function is indicated by  $G_b$  of GRU, and the mathematical equation is expressed in Equation (56).

$$\tilde{G}_b = \tan(wt^{FG}F_b + wt^{GG}(G_{b-1}rg_b)) \quad (55)$$

$$\begin{aligned} G_b &= (1 - ug_b) \oplus G_b + ug_b \oplus G_{b-1}G_b \\ &= (1 - ug_b) \oplus G_b + ug_b \oplus G_{b-1} \end{aligned} \quad (56)$$

Here, the developed O-SHO technique optimizes the number of hidden neurons of both CNN and RNN to improvise the classification accuracy.

## 5.7 | Operation of hybrid classification

The results obtained from both optimized CNN and RNN with the help of an optimized number of hidden neurons by O-DHOA are merged by the AND operation. The results of the RNN and the CNN undergo logical AND operation on each pair of input bits for performing the binary operations. The hybrid classifier considers two equal-length binary representations and therefore uses the result of both classifiers. This will provide the last output that produces two classes; one is normal and the other abnormal region.

# 6 | RESULTS AND DISCUSSIONS

## 6.1 | Experimental setup

The developed liver tumor segmentation and classification model was implemented on the MATLAB 2018a

software, and the performance evaluations were carried out. The dataset named LITS was used for the evaluation of the proposed liver tumor segmentation and classification. Also, the manually collected images were used for the analysis. The population size of the experiment was considered as 10, whereas the number of iterations was assumed to be 25. The performance analysis of the proposed O-SHO-CRNN (CNN + RNN) was compared over traditional PSO-CRNN,<sup>60</sup> GWO-CRNN,<sup>61</sup> WOA-CRNN,<sup>62</sup> and SHO-CRNN,<sup>18</sup> and the analysis was compared with traditional machine learning classifiers such as NN,<sup>63</sup> SVM,<sup>65</sup> NB,<sup>66</sup> and KNN<sup>67</sup> for the measures like “accuracy, sensitivity, specificity, precision, FPR, FNR, NPV, FDR, F1 score, and MCC.” The entire dataset has been divided into two parts, namely testing and training data. In the proposed system, the training data is varied from 25% to 85%, and the testing data is varied from 60% to 20%. i.e., when 40% of data is used for training the classifier, the remaining 60% of data is used for testing (validation) the performance of classifier, and the corresponding test results are plotted as graphs. The dataset comes from dramatic changes in population, contrast, scan range, pathology, and Field Of Vision (FOV). Most CT scans are pathological, including tumors of different sizes, metastases, and cysts. In order to improve the accuracy and reliability of the network for liver tumor segmentation, a new method, namely, O-SHO was proposed to perform the optimized segmentation and classification. The experimental results show that the overall accuracy attained by the proposed model is accurate, less sensitive to noise, and performs well superior on diverse CT images.

## 6.2 | Experimental results

Figure 6 shows the experimental results of the pre-processed images, liver segmented images, tumor segmented, and classifier tumor and non-tumor regions for the standard LITS dataset. Figure 7 provides the experimental results of the manually collected dataset. Here, the blue color represents the original tumor region, whereas the green color represents the segmented region of the non-tumor region.

## 6.3 | Performance analysis

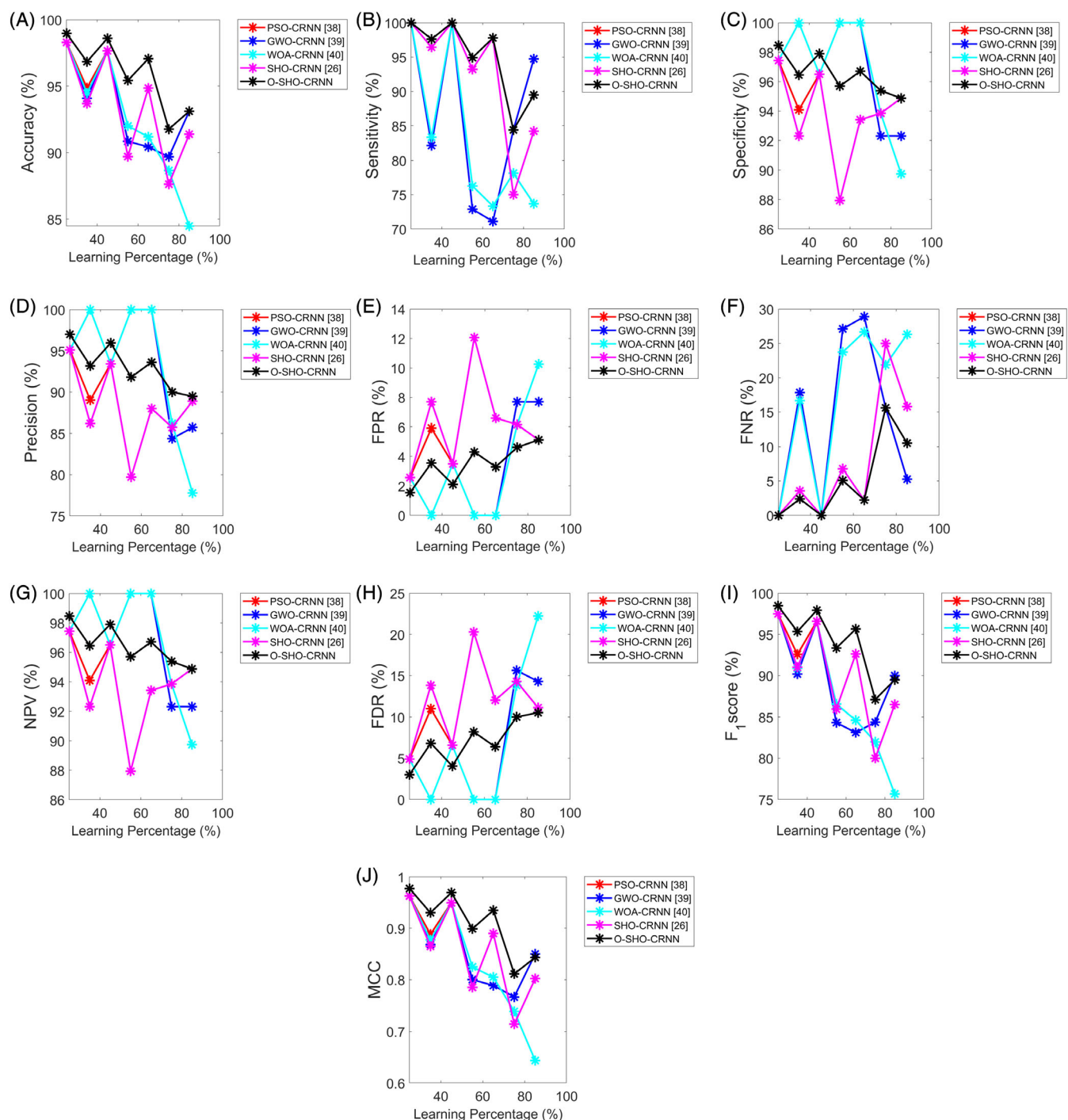
The performance analysis of the proposed and the state-of-the-art heuristic-based CRNN for learning percentages for various performance measures are shown in Figure 8 (From Figure 8A to J with each performance metric). From Figure 8A, the accuracy of the suggested O-SHO-CRNN is performing well when compared to

	Image 1	Image 2	Image 3	Image 4	Image 5
Original Images					
Pre-Processed Images					
Ground Truth Images					
Liver Segmented Images					
Tumor Segmented Images					
Tumor and Nontumor classification					

**FIGURE 6** Experimental results of the pre-processed images, liver segmented images, and tumor segmented images for LITS dataset [Color figure can be viewed at wileyonlinelibrary.com]

	Image 1	Image 2	Image 3	Image 4	Image 5	Image 6
Original Images						
Pre-Processed Images						
Ground Truth Images						
Liver Segmented Images						
Tumor Segmented Images						
Tumor and Nontumor classification						

**FIGURE 7** Experimental results of the pre-processed images, liver segmented images, and tumor segmented images for the manually collected dataset [Color figure can be viewed at wileyonlinelibrary.com]



**FIGURE 8** Performance analysis of the proposed and conventional heuristic-based CRNN for liver tumor segmentation and classification using LITS dataset for the measures: A, accuracy; B, sensitivity; C, specificity; D, precision; E, FPR; F, FNR; G, NPV; H, FDR; I, F<sub>1</sub> score; and J, MCC. FDR, false discovery rate; FNR, false negative rate; FPR, false positive rate; MCC, Matthew's correlation coefficient; NPV, negative predictive value [Color figure can be viewed at [wileyonlinelibrary.com](http://wileyonlinelibrary.com)]

conventional algorithms while considering all the learning percentages. At learning percentage 85, the accuracy of the improved O-SHO-CRNN is 1.6% upgraded than SHO-CRNN, and 10% upgraded than WOA-CRNN. Moreover, the sensitivity of the suggested O-SHO-CRNN is exactly defining the true observations from the entire

observations at all the learning percentages. In Figure 8B, the sensitivity of the developed O-SHO-CRNN is 1.5% better than SHO-CRNN, 16% better than WOA-CRNN, and 18.1% better than GWO-CRNN at learning percentage 35. From Figure 8D, the precision of the implemented O-SHO-CRNN has accurately defined the

true values for all the learning percentages. The precision of the developed O-SHO-CRNN is 5.2% improved than GWO-CRNN, and 16.8% improved than WOA-CRNN at a learning percentage 85. Also, the FNR of the improved O-SHO-CRNN is 37.5% enhanced than SHO-CRNN, 84.3% enhanced than WOA-CRNN, and 85.2% enhanced than GWO-CRNN at learning percentage 35 and it is depicted in Figure 8F. When considering the learning percentage as 35, the MCC of the implemented O-SHO-CRNN is 8.9% progressed than PSO-CRNN, 10.2% progressed than WOA-CRNN, and 12.7% progressed than GWO and SHO-CRNN, respectively. Therefore, the results have shown that the proposed O-SHO-CRNN is performing well for the segmentation and classification of liver tumor in a precise manner.

#### 6.4 | Analysis using machine learning algorithms

The analysis of the developed and the conventional machine learning models considering the learning percentages are shown in Figure 9 (From Figure 9A to J with each performance metric). The accuracy of the suggested O-SHO-CRNN has exactly identified the positive values from the entire values of all the learning percentages and it is shown in Figure 9A. It has 18.75% advanced than KNN, NB, and NN and 55.7% advanced than SVM at a learning percentage 85. In Figure 9D, the precision of the presented O-SHO-CRNN is exactly recognized as the true observations at all learning percentages. When considering the learning percentage as 35, the precision of the proposed O-SHO-CRNN is 15% superior to KNN, 13.5% superior to NB and NN, and 26% superior to SVM. At all learning percentages, the FPR of the implemented O-SHO-CRNN is exactly computed. In Figure 9E, the FPR of the suggested O-SHO-CRNN is 50% better than KNN, NB, and NN, and 83.3% better than SVM at learning percentage 75. For the learning percentage as 35, the F1 score of the recommended O-SHO-CRNN is 13% upgraded than KNN, 11.7% upgraded than NB and NN, and 15.8% upgraded than SVM and it is shown in Figure 9I. Thus, the proposed O-SHO-CRNN is well suitable for classifying the tumor region from the liver CT images.

#### 6.5 | Analysis using deep learning algorithms

The classification analysis of the introduced and the conventional deep learning methods with respect to learning percentages are given in Figure 10 (From Figure 10A to J

with each performance metric). From Figure 10A, the accuracy of the proposed O-SHO-CRNN has been defined precisely to all the learning percentages. At learning percentage 85, the accuracy of the improved O-SHO-CRNN is 24% better than CRNN and RNN, and 55% better than CNN. At all learning percentages, the precision of the implemented O-SHO-CRNN is performing well. In Figure 10D, the precision of the modified O-SHO-CRNN is 45.1% superior to CRNN and RNN, and 100% superior to CNN at learning percentage 35. The NPV of the presented O-SHO-CRNN has identified the negative values exactly. At learning percentage 35, the NPV of the suggested O-SHO-CRNN is 3.2% advanced than CRNN, 4.3% advanced than RNN, and 7.8% advanced than CNN, and it is shown in Figure 10G. Moreover, the FDR of the proposed O-SHO-CRNN at learning percentage 35 is 22.2% improved than CRNN, 30% improved than RNN, and 56.2% improved than CNN. Therefore, the performance of the proposed O-SHO-CRNN model is accurate when compared to other deep learning models in classifying liver tumor from liver CT images.

#### 6.6 | Overall performance analysis on LITS dataset

The overall performance analysis of the proposed and the conventional models are shown in Tables 2, 3, and 4. The performance analysis of the developed O-SHO-CRNN and the traditional CRNN models is shown in Table 2. Here, the accuracy of the suggested O-SHO-CRNN is 12.5% better than PSO-CRNN and SHO-CRNN, and 8% better than WOA-CRNN. Moreover, the performance analysis of the developed O-SHO-CRNN and traditional classifiers are given in Table 3. The accuracy of the introduced O-SHO-CRNN is better than other techniques. It is 4.7% advanced than NN, 21.9% advanced than SVM, 7.2% advanced than NB, and KNN. Also, the overall performance of the developed O-SHO-CRNN and classical deep learning models is tabulated in Table 4. From Table 4, the accuracy of the introduced O-SHO-CRNN is 18.6% superior to CNN, 3.4% superior to RNN, and 2.2% superior to CRNN. Finally, it is concluded that the proposed O-SHO-CRNN is well suitable for accurate liver segmentation and classification.

#### 6.7 | Analysis on manually collected data

The overall analysis of the proposed and conventional models for the manually collected dataset is given in Tables 5, 6, and 7. From Table 5, the accuracy of the proposed O-SHO-CRNN for heuristic-based CRNN for liver

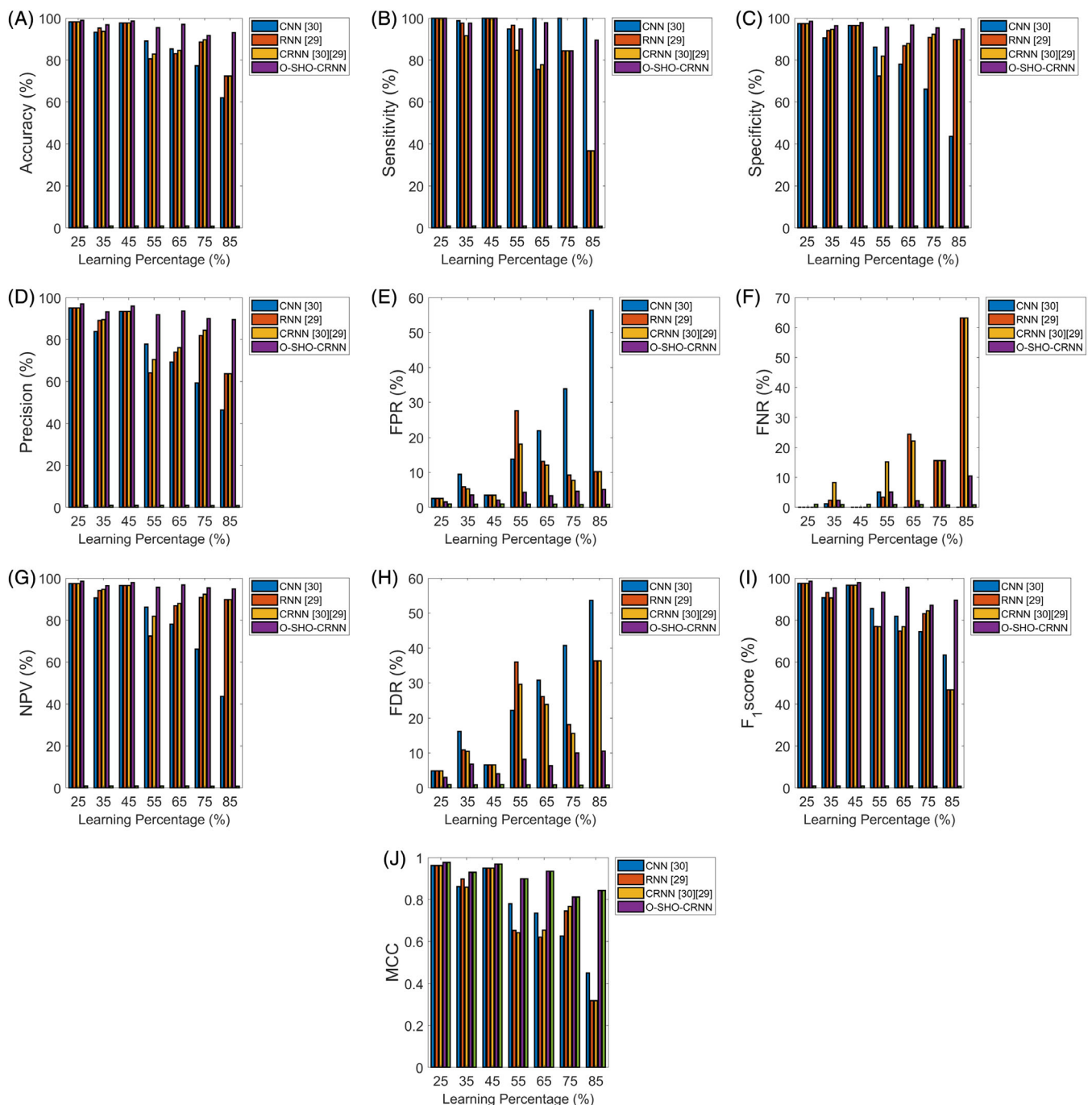


**FIGURE 9** Classification analysis of the proposed and machine learning models for liver tumor segmentation and classification using LITS dataset for the measures: A, accuracy; B, sensitivity; C, specificity; D, precision; E, FPR; F, FNR; G, NPV; H, FDR; I, F1 score; and J, MCC. FDR, false discovery rate; FNR, false negative rate; FPR, false positive rate; MCC, Matthew's correlation coefficient; NPV, negative predictive value [Color figure can be viewed at wileyonlinelibrary.com]

tumor segmentation and classification is 16.67% advanced than PSO-CRNN, 0.01% advanced than GWO-CRNN, 16.67% advanced than WOA-CRNN and 16.67% advanced than SHO-CRNN. On considering Table 6, the accuracy of the proposed O-SHO-CRNN with respect to deep learning models for liver tumor segmentation and

classification is 0.01% progressed than CNN, 0.01% progressed than RNN and 16.67% progressed than RNN. In Table 7, the accuracy of the proposed O-SHO-CRNN with respect to machine learning models for liver tumor segmentation and classification is 16.67% superior to NN, 85.71% superior to SVM, 16.67% superior to NB, and

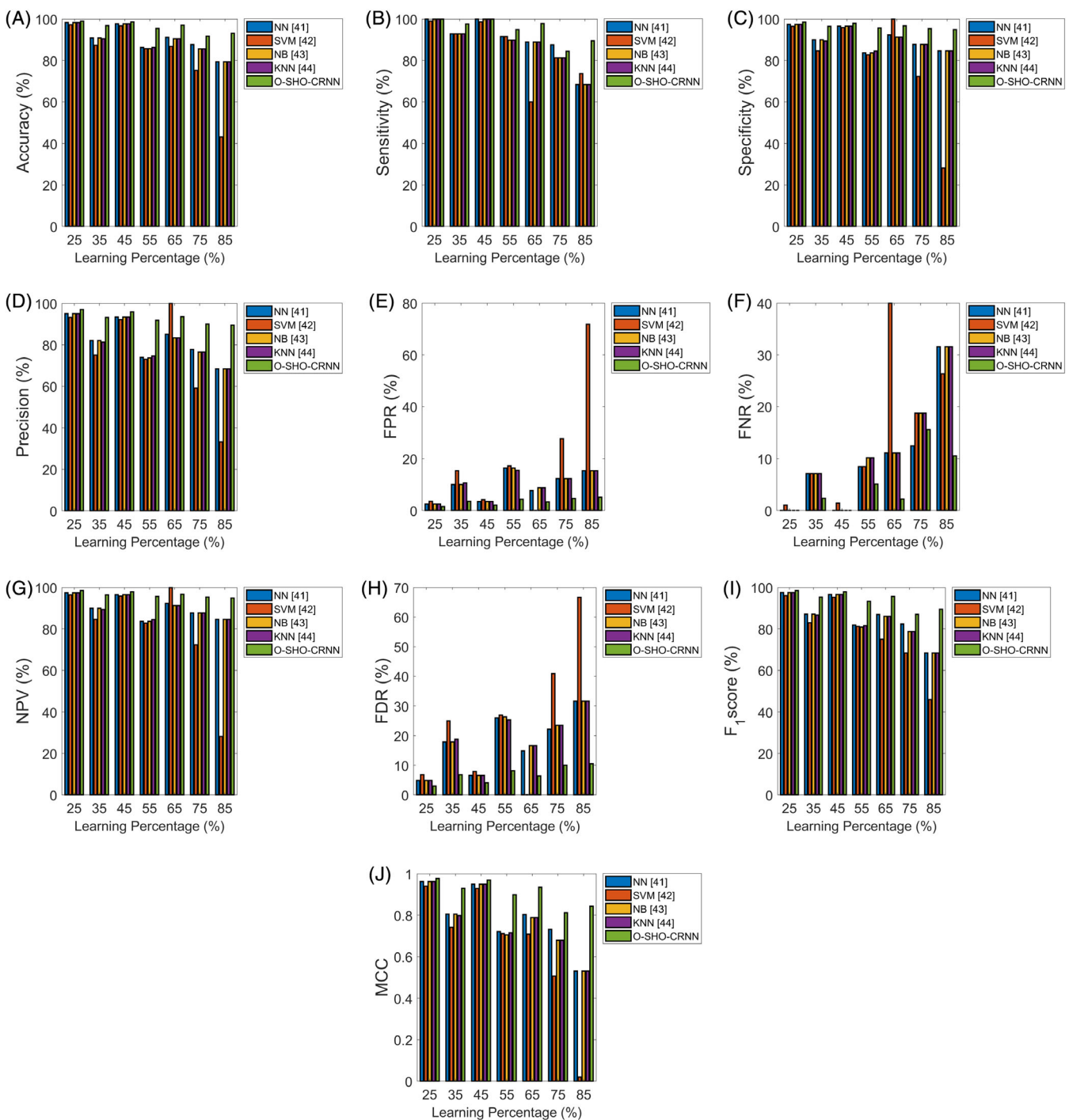


**FIGURE 10** Classification analysis of the proposed and deep learning models for liver rumor segmentation and classification using LITS dataset for the measures: A, accuracy; B, sensitivity; C, specificity; D, precision; E, FPR; F, FNR; G, NPV; H, FDR; I, F<sub>1</sub> score; and J, MCC. FDR, false discovery rate; FNR, false negative rate; FPR, false positive rate; MCC, Matthew's correlation coefficient; NPV, negative predictive value [Color figure can be viewed at [wileyonlinelibrary.com](http://wileyonlinelibrary.com)]

16.67% superior to KNN. Thus, it can be concluded that the proposed O-SHO-CRNN in case of analysis on manually collected data performs well when it is compared with state-of-the-art methods.

## 6.8 | Comparative analysis

Here, the proposed O-SHO-CRNN-based liver tumor segmentation and classification is compared with the

**TABLE 2** Overall Performance Analysis of the proposed and conventional heuristic-based CRNN for liver tumor segmentation and classification using LITS dataset

Performance measures	PSO-CRNN <sup>60</sup>	GWO-CRNN <sup>61</sup>	WOA-CRNN <sup>62</sup>	SHO-CRNN <sup>18</sup>	O-SHO-CRNN
Accuracy	0.75	0.84375	0.78125	0.75	0.84375
Sensitivity	0.93846	0.92308	0.93846	0.93846	0.95385
Specificity	0.85714	0.84375	0.86207	0.85714	0.9
Precision	0.061538	0.076923	0.061538	0.061538	0.046154
FPR	0.25	0.15625	0.21875	0.25	0.15625
FNR	0.93846	0.92308	0.93846	0.93846	0.95385
NPV	0.14286	0.15625	0.13793	0.14286	0.1
FDR	0.8	0.84375	0.81967	0.8	0.87097
F1-score	0.71434	0.76683	0.73916	0.71434	0.81137
MCC	0.75	0.84375	0.78125	0.75	0.84375

**TABLE 3** Overall classification analysis of the proposed and machine learning models for liver tumor segmentation and classification using LITS dataset

Performance measures	NN <sup>63</sup>	SVM <sup>65</sup>	NB <sup>66</sup>	KNN <sup>67</sup>	O-SHO-CRNN
Accuracy	0.87629	0.75258	0.85567	0.85567	0.91753
Sensitivity	0.875	0.8125	0.8125	0.8125	0.84375
Specificity	0.87692	0.72308	0.87692	0.87692	0.95385
Precision	0.77778	0.59091	0.76471	0.76471	0.9
FPR	0.12308	0.27692	0.12308	0.12308	0.046154
FNR	0.125	0.1875	0.1875	0.1875	0.15625
NPV	0.87692	0.72308	0.87692	0.87692	0.95385
FDR	0.22222	0.40909	0.23529	0.23529	0.1
F1-score	0.82353	0.68421	0.78788	0.78788	0.87097
MCC	0.73179	0.50581	0.67937	0.67937	0.81137

**TABLE 4** Overall classification analysis of the proposed and conventional deep learning models for liver tumor segmentation and classification using LITS dataset

Performance measures	CNN <sup>58</sup>	RNN <sup>59</sup>	CRNN <sup>58,59</sup>	O-SHO-CRNN
Accuracy	0.7732	0.8866	0.89691	0.91753
Sensitivity	1	0.84375	0.84375	0.84375
Specificity	0.66154	0.90769	0.92308	0.95385
Precision	0.59259	0.81818	0.84375	0.9
FPR	0.33846	0.092308	0.076923	0.046154
FNR	0	0.15625	0.15625	0.15625
NPV	0.66154	0.90769	0.92308	0.95385
FDR	0.40741	0.18182	0.15625	0.1
F1-score	0.74419	0.83077	0.84375	0.87097

state-of-the-art classifiers such as CNN,<sup>1</sup> SFPC,<sup>5</sup> and DT,<sup>6</sup> which is shown in Tables 8 and 9. From Table 8 for LITS dataset, the accuracy of the developed O-SHO-CRNN is labeled in a precise manner. It is 14.10% superior to CNN, 1.13% superior to SFPC, and 8.53% superior to DT. In addition, the specificity of the suggested O-SHO-CRNN has correctly identified the true observations.

Here, the specificity of the developed O-SHO-CRNN is 21.5% better than CNN, 8.77% better than SFPC, and 24% better than DT. In Table 9, on considering the manually collected dataset, the FDR of the suggested O-SHO-CRNN is 1.07% improved than CNN, 6.84% improved than SFPC, and 4.21% improved than DT. Here, the MCC of the developed O-SHO-CRNN is 9.02% better than

**TABLE 5** Overall analysis of the proposed and conventional heuristic-based CRNN for liver tumor segmentation and classification using manually collected dataset

Performance measures	PSO-CRNN <sup>60</sup>	GWO-CRNN <sup>61</sup>	WOA-CRNN <sup>62</sup>	SHO-CRNN <sup>18</sup>	O-SHO-CRNN
Accuracy	0.75	0.875	0.75	0.75	0.875
Sensitivity	0.5	0.5	0	0.5	1
Specificity	0.83333	1	1	0.83333	0.83333
Precision	0.5	1	0	0.5	0.66667
FPR	0.16667	0	0	0.16667	0.16667
FNR	0.5	0.5	1	0.5	0
NPV	0.83333	1	1	0.83333	0.83333
FDR	0.5	0	0	0.5	0.33333
F1-score	0.5	0.66667	0	0.5	0.8
MCC	0.33333	0.65465	0	0.33333	0.74536

Performance measures	CNN <sup>58</sup>	RNN <sup>59</sup>	CRNN <sup>58,59</sup>	O-SHO-CRNN
Accuracy	0.875	0.875	0.75	0.875
Sensitivity	0.5	0.5	0	1
Specificity	1	1	1	0.83333
Precision	1	1	0	0.66667
FPR	0	0	0	0.16667
FNR	0.5	0.5	1	0
NPV	1	1	1	0.83333
FDR	0	0	0	0.33333
F1-score	0.66667	0.66667	0	0.8
MCC	0.65465	0.65465	0	0.74536

Performance measures	NN <sup>63</sup>	SVM <sup>64</sup>	NB <sup>65</sup>	KNN <sup>66</sup>	O-SHO-CRNN
Accuracy	0.75	0.125	0.75	0.75	0.875
Sensitivity	0	0	1	1	1
Specificity	1	0.16667	0.66667	0.66667	0.83333
Precision	0	0	0.5	0.5	0.66667
FPR	0	0.83333	0.33333	0.33333	0.16667
FNR	1	1	0	0	0
NPV	1	0.16667	0.66667	0.66667	0.83333
FDR	0	1	0.5	0.5	0.33333
F1-score	0	0	0.66667	0.66667	0.8
MCC	0	-0.74536	0.57735	0.57735	0.74536

CNN, 2.17% better than SFPC, and 17.8% better than DT. Hence, it is confirmed that the improved O-SHO-CRNN is effective for liver tumor segmentation and classification when compared with literal works.

## 6.9 | Analysis of computational time

The computational time of the proposed and existing methods is analyzed and listed in Table 10. The

**TABLE 6** Overall analysis of the proposed and conventional deep learning models for liver tumor segmentation and classification using manually collected dataset**TABLE 7** Overall analysis of the proposed and conventional machine learning models for liver tumor segmentation and classification using manually collected dataset

**TABLE 8** Comparative analysis of the proposed model with literature works for liver tumor segmentation and classification using LITS dataset

Performance measures	CNN <sup>6</sup>	SFPC <sup>19</sup>	DT <sup>21</sup>	O-SHO-CRNN
Accuracy	0.80412	0.90722	0.84536	0.91753
Sensitivity	0.84375	0.96875	1	0.84375
Specificity	0.78462	0.87692	0.76923	0.95385
Precision	0.65854	0.79487	0.68085	0.9
FPR	0.21538	0.12308	0.23077	0.046154
FNR	0.15625	0.03125	0	0.15625
NPV	0.78462	0.87692	0.76923	0.95385
FDR	0.34146	0.20513	0.31915	0.1
F1-score	0.73973	0.87324	0.81013	0.87097
MCC	0.59808	0.81094	0.72369	0.81137

**TABLE 9** Comparative analysis of the proposed model with literature works for liver tumor segmentation and classification using manually collected dataset

Performance measures	CNN <sup>6</sup>	SFPC <sup>19</sup>	DT <sup>21</sup>	O-SHO-CRNN
Accuracy	0.5	0.5	0.25	0.875
Sensitivity	1	1	1	1
Specificity	0.72395	0.78236	0.69729	0.83333
Precision	0.33333	0.33333	0.25	0.66667
FPR	0.66667	0.66667	1	0.16667
FNR	0.34146	0.20513	0.31915	0.15637
NPV	0.73945	0.79218	0.75295	0.83333
FDR	0.32978	0.35783	0.31986	0.33333
F1-score	0.5	0.5	0.4	0.8
MCC	0.68367	0.72946	0.63273	0.74536

**TABLE 10** Computational time of the proposed and existing methods for liver tumor classification

Methods	Computational time (s)
NN <sup>41</sup>	0.34432
SVM <sup>42</sup>	1.9264
NB <sup>43</sup>	0.14255
KNN <sup>44</sup>	0.04547
PSO-CRNN <sup>38</sup>	11.367
GWO-CRNN <sup>39</sup>	3.2945
WOA-CRNN <sup>40</sup>	1.8936
SHO-CRNN <sup>26</sup>	1.2441
DT <sup>6</sup>	0.10003
CNN <sup>30</sup>	1.5755
RNN <sup>29</sup>	1.0099
CRNN <sup>3029</sup>	0.52678
O-SHO-CRNN	1.8068

computational time of the proposed O-SHO-CRNN is 80.9% worst than NN, 6.20% better than SVM, 92.1% worst than NB, 97.4% worst than KNN, 84.1% better than PSO-CRNN, 45.1% better than GWO-CRNN, 4.58% better than WOA-CRNN, 45.2% worst than SHO-CRNN, 94.4% worst than DT, 14.6% worst than CNN, 78.9% worst than RNN, and 70.8% worst than CRNN respectively. Even though the computational time of the existing method is worst than some of the methods, the performance in segmentation and classification seems to be better when compared to all the existing methods.

## 7 | CONCLUSION

This article has presented a new model, namely O-SHO for liver tumor segmentation and classification. The developed model consists of five phases such as “pre-processing, liver segmentation, tumor segmentation,

feature extraction, and classification." Initially, the collected CT images were pre-processed by two steps, such as histogram equalization, and median filtering mechanism. Once pre-processing was performed, the liver was segmented from the abdominal images by the adaptive thresholding and level set segmentation. In addition, an improved model called Fuzzy Centroid-based optimized region growing algorithm with tolerance optimization was utilized to perform the tumor segmentation. Later, three sets of features namely LBP, GLCM, and shape features were extracted from the pre-processed images. Furthermore, the classification was performed by merging deep learning models like RNN and CNN. Here, the optimization of hidden neurons was performed by the proposed Fuzzy Centroid-based optimized region growing algorithm. From the experimental results, the accuracy of the suggested O-SHO-CRNN was 12.5% better than PSO-CRNN and SHO-CRNN, and 8% better than WOA-CRNN. From the experimental results, it is confirmed that the proposed O-SHO is outperforming the conventional models in liver tumor classification. The proposed method was efficient while maintaining accuracy. Such a fast segmentation method might be used for practical applications like trajectory planning for radiofrequency ablation without significantly increasing the processing time, which involves segmentations of all relevant organs/structures. In addition, liver tumor segmentation, and classification also offers several real-time applications for treatment planning, such as Thermal Percutaneous Ablation, Percutaneous Ethanol Injection (PEI), Radiotherapy Surgical Resection, and Arterial Embolization. Furthermore, in treatments such as Selective Internal Radiation Therapy (SIRT), fractional dose calculation of the liver and tumors depend on the volume of the liver and tumors. Hence, to calculate the dose delivered to the tumor, it is essential to segment the tumor from the background and calculate the volume of the tumor region, and it has been left for the suggestion of the future work.

## ORCID

Munipraveena Rela  <https://orcid.org/0000-0002-6494-6722>

## REFERENCES

1. Siegel R, Ma J, Zou Z, Jemal A. Cancer statistics, 2014. *CA Cancer J Clin.* 2014;64(1):9-29.
2. Damhorst GL, Murtagh M, Rodriguez WR, Bashir R. Microfluidics and nanotechnology for detection of global infectious diseases. *Proc IEEE.* 2015;103(2):150-160.
3. Murakami T, Imai Y, Okada M, et al. Ultrasonography, computed tomography and magnetic resonance imaging of hepatocellular carcinoma: toward improved treatment decisions. *Oncology.* 2011;81:86-99.
4. Ranjbarzadeh R, Saadi SB. Automated liver and tumor segmentation based on concave and convex points using fuzzy c-means and mean shift clustering. *Measurement.* 2020;150.
5. Hou W, Tan BT, Abdullah LN, et al. Nanodiamond-manganese dual mode MRI contrast agents for enhanced liver tumor detection. *Nanomed Nanotechnol Biol Med.* 2017;13(3):783-793.
6. Dogantekin A, Ozyurt F, Avci E, Koc M. A novel approach for liver image classification: PH-C-ELM. *Measurement.* 2019;137:332-338.
7. Nasim Nasiri, mir Hossein Foruzan, and Yen-Wei Chen, "Integration of a knowledge-based constraint into generative models with applications in semi-automatic segmentation of liver tumors", *Biomed Signal Process Control*, 2020;57:1-11.
8. Lebre M-A, Vacavant A, Brochier MG, et al. Automatic segmentation methods for liver and hepatic vessels from CT and MRI volumes, applied to the Couinaud scheme. *Comput Biol Med.* 2019;110:42-51.
9. Xu L, Zhu Y, Zhang Y, Yang H. Liver segmentation based on region growing and level set active contour model with new signed pressure force function. *Optik.* 2020;202.
10. Patil DD, Deore SG. Medical image segmentation: a review. *Int J Comput Sci Mobile Comput.* 2013;2(1):22-27.
11. Cheng D, Guot Y, Zhang Y. A novel image segmentation approach based on neutrosophic set and improved fuzzy C-means algorithm. *New Math Nat Comput.* 2011;7(1):155-171.
12. Budak U, Guo Y, Tanyildizi E, Şengür A. Cascaded deep convolutional encoder-decoder neural networks for efficient liver tumor segmentation. *Med Hypotheses.* 2020;134:1-8.
13. Baazaoui A, Barhoumi W, Ahmed A, Zagrouba E. Semi-automated segmentation of single and multiple Tumors in liver CT images using entropy-based fuzzy region growing. *IRBM.* 2017;38(2):98-108.
14. Tanaka O, Kojima T, Ohbora A, et al. Scores of Child-Pugh Classification Impact Overall Survival after Stereotactic Body Radiation Therapy for Primary and Metastatic Liver tumors. *J Clin Exp Hepatol.* 2019;10(2):101-105.
15. Perell K, Vincent M, Vainer B, et al. Development and validation of a micro RNA based diagnostic assay for primary tumor site classification of liver core biopsies. *Mol Oncol.* 2015;9(1):68-77.
16. Gaitanidis A, Alevizakos M, Tsaroucha A, Simopoulos C, Pitiakoudis M. Incidence and predictors of synchronous liver metastases in patients with gastrointestinal stromal tumors (GISTS). *Am J Surg.* 2018;216(3):492-497.
17. Li J, Wu Y, Shen N, et al. A Fully Automatic Computer-Aided Diagnosis System for Hepatocellular Carcinoma Using Convolutional Neural Networks. *Biocybernet Biomed Eng.* 2019;40(1):238-248.
18. Lin C, Dai H, Hong X, et al. The prognostic impact of primary tumor resection in pancreatic neuroendocrine tumors with synchronous multifocal liver metastases. *Pancreatology.* 2018;18(5):608-614.
19. Smeets D, Loockx D, Stijnen B, De Dobbelaer B, Vandermeulen D, Suetens P. Semi-automatic level set segmentation of liver tumors combining a spiral-scanning technique with supervised fuzzy pixel classification. *Med Image Anal.* 2010;14(1):13-20.

20. Chang C-C, Chen H-H, Chang Y-C, et al. Computer-aided diagnosis of liver tumors on computed tomography images. *Comput Methods Programs Biomed*. 2017;145:45-51.
21. Das A, Das P, Panda SS, Sabut S. Detection of liver cancer using modified fuzzy clustering and decision tree classifier in CT images. *Math Method Pat Recognit*. 2019;29(2):201-211.
22. Chaieb F, Said TB, Mabrouk S, Ghorbel F. Accelerated liver tumor segmentation in four-phase computed tomography images. *J Real-Time Image Process*. 2017;13(1):121-133.
23. Kang JH, Kim SH, Han JK. Poorly-differentiated colorectal neuroendocrine tumor: CT differentiation from well-differentiated neuroendocrine tumor and poorly-differentiated adenocarcinomas. *Eur Radiol*. 2017;27:3867-3876.
24. Anter AM, Hassenian AE. Computational intelligence optimization approach based on particle swarm optimizer and neutrosophic set for abdominal CT liver tumor segmentation. *J Comput Sci*. 2018;25:376-387.
25. Zheng S, Fang B, Li L, Gao M, Wang Y, Peng K. Automatic liver tumor segmentation in CT combining FCN and NMF-based deformable odel. *Comput Methods Biomech Biomed Eng Imaging Vis*. 2019;1:10.
26. Anter AM, Hassenian AE. CT liver tumor segmentation hybrid approach using neutrosophic sets, fast fuzzy c-means and adaptive watershed algorithm. *Artif Intell Med*. 2019;97:105-117.
27. Bai Z, Jiang H, Li S, Yao Y. Liver tumor segmentation based on multi-scale candidate generation and fractal residual network. *IEEE Access*. 2019;7:82122-82133.
28. Dhiman G, Kumar V. Spotted hyena optimizer: a novel bio-inspired based metaheuristic technique for engineering applications. *Adv Eng Softw*. 2017;114:48-70.
29. Dhiman G, Kumar V. Emperor penguin optimizer: a bio-inspired algorithm for engineering problems. *Knowl-Based Syst*. 2018;159:20-50.
30. Dhiman G, Kumar V. Multi-objective spotted hyena optimizer: a multi-objective optimization algorithm for engineering problems. *Knowl-Based Syst*. 2018;150:175-197.
31. Singh P, Dhiman G. A hybrid fuzzy time series forecasting model based on granular computing and bio-inspired optimization approaches. *J Comput Sci*. 2018;27:370-385.
32. Dhiman G, Kaur A. Spotted Hyena Optimizer for Solving Engineering Design Problems, 2017 International Conference on Machine learning and Data Science; 2018.
33. Dhiman G, Kumar V. Seagull optimization algorithm: theory and its applications for large-scale industrial engineering problems. *Knowl-Based Syst*. 2019;165:169-196.
34. Dhiman G, Kumar V. Spotted hyena optimizer for solving complex and non-linear constrained engineering problems. *Adv Intell Syst Comput*. 2018;741:857-867.
35. Singh P, Dhiman G. Uncertainty representation using fuzzy-entropy approach: special application in remotely sensed high-resolution satellite images (RSHRSIs). *Appl Soft Comput*. 2018;72:121-139.
36. Dhiman G, Kaur A. A hybrid algorithm based on particle swarm and spotted hyena optimizer for global optimization. *Soft Comput Probl Solv*. 2018;816:599-615.
37. Dhiman G, Kaur A. Optimizing the design of airfoil and optical buffer problems using spotted hyena optimizer. *Designs*. 2018;1:16.
38. Kaur A, Kaur S, Dhiman G. A quantum method for dynamic nonlinear programming technique using Schrodinger equation and Monte Carlo approach. *Mod Phys Lett B*. 2018;32(30):1-12.
39. Singh P, Dhiman G, Kaur A. A quantum approach for time series data based on graph and Schrodinger equations methods. *Mod Phys Lett A*. 2018;33(35):1-23.
40. Dhiman G, Kumar V. Astrophysics inspired multi-objective approach for automatic clustering and feature selection in real-life environment. *Mod Phys Lett B*. 2018;32(31):1-23.
41. Dhiman G, Guo S, Kaur S. ED-SHO: a framework for solving nonlinear economic load power dispatch problem using spotted hyena optimizer. *Mod Phys Lett A*. 2018;33(40):1-14.
42. Dhiman G, Kaur A. STOA: a bio-inspired based optimization algorithm for industrial engineering problems. *Eng Appl Artif Intel*. 2019;82:148-174.
43. Dhiman G. ESA: a hybrid bio-inspired metaheuristic optimization approach for engineering problems. *Eng Comput*. 2019.
44. Dhiman G. MOSHEPO: a hybrid multi-objective approach to solve economic load dispatch and micro grid problems. *Appl Intell*. 2019;50(4):119-137.
45. Dehghani M, Montazeri Z, Malik OP, Dhiman G, Kumar V. BOSA: binary orientation search algorithm. *Int J Innov Technol Explor Eng*. 2019;9(1):5306-5310.
46. Singh P, Dhiman G, Guo S, et al. A hybrid fuzzy quantum time series and linear programming model: special application on TAIEX index dataset. *Mod Phys Lett A*. 2019;34(25):1-20.
47. Garg M, Dhiman G. Deep convolution neural network approach for defect inspection of textured surfaces. *J Inst Electron Comput*. 2020;2:28-38.
48. Dhiman, Gaurav. *Multi-objective metaheuristic approaches for data clustering in engineering application(s)*. TIET Digital Repository; 2019.
49. Kaur S, Awasthi LK, Sangal AL, Dhiman G. Tunicate swarm algorithm: a new bio-inspired based metaheuristic paradigm for global optimization. *Eng Appl Artif Intell*. 2020;90:1-29.
50. Dorothy R, Joany RM, Rathish J, Santhana Prabha S, Rajendran S, Joseph ST. Image enhancement by histogram equalization. *Int J Nano Corros Sci Eng*. 2015;2:21-30.
51. Zhu Y, Cheng H. An improved median filtering algorithm for image noise reduction. *Phys Procedia*. 2012;25:609-616.
52. Patil MP, Ratnaparkhe VR, Kakarwal SN. Adaptive thresholding for image enhancement: hardware approach. *Int J Eng Res Technol*. 2015;3(1):141-150.
53. Jiang X, Zhang R, Nie S. Image segmentation based on level set method. *Phys Procedia*. 2012;33:840-845.
54. Feng Q, Gao B, Lu P, et al. Automatic seeded region growing for thermography debonding detection of CFRP. *NDT & E Int*. 2018;99:36-49.
55. Celik T, Lee HK. Comments on “a robust fuzzy local information C-means clustering algorithm”. *IEEE Trans Image Process*. 2013;22(3):1258-1261.
56. Liao S, Law MWK, Chung ACS. Dominant local binary patterns for texture classification. *IEEE Trans Image Process*. 2009;18(5):1107-1118.
57. Swamy SM, Rajakumar BR, Valarmathi IR, Design of Hybrid Wind and Photovoltaic Power System using Opposition-based Genetic Algorithm with Cauchy Mutation, IET Chennai Fourth International Conference on Sustainable Energy and Intelligent Systems (SEISCON 2013), Chennai, India; 2013.

58. Ivars Namatēvs, "Deep convolutional neural networks: structure, feature extraction and training", *Inform Technol Manag Sci*, December 2017;20:40-47.
59. Li F, Liu M. A hybrid convolutional and recurrent neural network for hippocampus analysis in Alzheimer's disease. *J Neurosci Methods*. 2019;323:108-118.
60. Pedersen MEH, Chipperfield AJ. Simplifying particle swarm optimization. *Appl Soft Comput*. 2010;10(2):618-628.
61. Mirjalili S, Mirjalili SM, Lewis A. Grey wolf optimizer. *Adv Eng Softw*. 2014;69:46-61.
62. Mirjalili S, Lewis A. The whale optimization algorithm. *Adv Eng Softw*. 2016;95:51-67.
63. Fernández-Navarro F, Carbonero-Ruz M, Becerra Alonso D, Torres-Jiménez M. Global sensitivity estimates for neural network classifiers. *IEEE Trans Neural Netw Learn Syst*. 2017;28(11):2592-2604.
64. Marsaline Beno M, Valarmathi IR, Swamy SM, Rajakumar BR. Threshold prediction for segmenting tumor from brain MRI scans. *Int J Imaging Syst Technol*. 2014;24(2):129-137.
65. Yu S, Tan KK, Sng BL, Shengjin L, Sia ATH. Lumbar ultrasound image feature extraction and classification with support vector machine. *Ultrasound Med Biol*. 2015;41(10):2677-2689.
66. Sanchis A, Juan A, Vidal E. A word-based Naïve Bayes classifier for confidence estimation in speech recognition. *IEEE Trans Audio Speech Lang Process*. 2012;20(2):565-574.
67. Chen Y, Hu X, Fan W, et al. Fast density peak clustering for large scale data based on kNN. *Knowledge-Based Systems*. 2019;187:1-7.

**How to cite this article:** Rela M, Nagaraja Rao S, Ramana Reddy P. Optimized segmentation and classification for liver tumor segmentation and classification using opposition-based spotted hyena optimization. *Int J Imaging Syst Technol*. 2021;31: 627-656. <https://doi.org/10.1002/ima.22519>